International Journal of Coal Geology 303 (2025) 104739

Contents lists available at ScienceDirect

International Journal of Coal Geology

journal homepage: www.elsevier.com/locate/coal

Implications of solid bitumen association with low- to medium-temperature hydrothermal minerals in hydrocarbon reservoirs of Southwest China: Insights from organic petrology and sulfur isotopes

Wen Sun [a,b], Ningning Zhong [a,b,*], Yongli Lu [b], Dahua Li [c], Qingyong Luo [b], Lipeng Yao [d], Yanan Yang [b], Chunfang Cai [b], Zilong Fang [b]

[a] Key Laboratory of Shale Gas Exploration, Ministry of Natural Resources, China University of Petroleum (Beijing), Beijing 102249, China
[b] College of Geosciences, China University of Petroleum (Beijing), Beijing 102249, China
[c] Key Laboratory of Shale Gas Exploration, Ministry of Natural Resources (Chongqing Institute of Geology and Mineral Resources), Chongqing 401120, China
[d] Key Laboratory of Environment Change and Resources Use in Beibu Gulf, Ministry of Education, Nanning Normal University, Nanning 530001, China

ARTICLE INFO

Keywords:
Solid bitumen
Metal sulfide minerals
Sulfur isotopes
Organic-inorganic interactions
Metallogeny
Paleo-oil reservoir reconstruction
Southwest China

ABSTRACT

Solid bitumen in Southwest China often coexists with metal deposits, indicating a genetic link between organic matter and ore formation. However, this linkage remains underexplored. This study investigated the relationship between sulfur origin and organic matter maturity through sulfur isotopes of metal sulfides. Organic petrology revealed that solid bitumen associated with minerals exhibited stronger optical anisotropy (ΔBRo >3.32 %) and higher S/C atomic ratios (0.029–0.033) than non-associated bitumen (0.005–0.021). Fluid inclusion analysis showed that ore-stage calcite inclusions have higher homogenization temperatures than those in paleo-oil reservoirs, indicating that ore-forming processes accelerated hydrocarbon thermal evolution. Solid bitumen-mineral associations were classified into Mississippi Valley-type (MVT), stratiform mercury, and disseminated gold deposits. Sulfur isotope compositions identified three sulfur sources: bacterial sulfate reduction (BSR), thermochemical sulfate reduction (TSR), and thermal decomposition of sulfur-containing organic matter (TDS). In the Lanping-Simao Basin, $\delta^{34}S_{CDT}$ values below 0 ‰ suggest sulfur derived from BSR, with hydrocarbons contributing reduced sulfur. In the Xuefeng Mountains Uplift, $\delta^{34}S_{CDT}$ values exceeding 20 ‰ indicate TSR-driven sulfur, with metallogeny enhancing hydrocarbon accumulation and mineralization. In the Kangdian Axis, $\delta^{34}S_{CDT}$ values under 20 ‰ suggest sulfur from TSR and TDS, with mineralization causing oil cracking and reservoir destruction. The findings demonstrate that metallogeny accelerates organic matter maturation, reshapes reservoirs, and drives oil cracking. Simultaneously, organic-inorganic interactions govern metal sulfide formation and precipitation, underscoring their critical role in ore genesis.

1. Introduction

Solid bitumen is widely distributed in Southwest China and coexists with low- to medium-temperature hydrothermal deposits and minerals. Globally, extensive clusters of low- to medium-temperature ore deposits are found in only two regions: the midwestern United States (Kesler et al., 1994; Sverjensky, 1986) and Southwest China (Huang et al., 2011). Solid bitumen in reservoirs is a (semi)solid, opaque, amorphous organic mass formed by the alteration of liquid petroleum that migrates or becomes trapped within carbonate and siliciclastic reservoirs (Rogers et al., 1974; Sanei, 2020). Low- to medium-temperature hydrothermal minerals are those formed at temperatures below 200 °C and include sulfide ores such as Mississippi Valley-type (MVT) lead–zinc ores, Carlin-type gold ores, and stratiform mercury ores, which are the focus of this research.

Numerous low- to medium-temperature hydrothermal deposits exhibit a distinct spatiotemporal coexistence with paleo-oil reservoirs (Gu et al., 2010; Sverjensky, 1986). Since the 1980s, researchers have recognized that large-scale mineral deposits may be closely associated with the involvement of organic matter (Sverjensky, 1986). Hydrocarbons may play a significant role as reducing agents in metallogenesis (Greenwood et al., 2018), either by directly contributing to sulfate

* Corresponding author at: Key Laboratory of Shale Gas Exploration, Ministry of Natural Resources, China University of Petroleum (Beijing), Beijing 102249, China
E-mail address: nnzhongxp@cup.edu.cn (N. Zhong).

https://doi.org/10.1016/j.coal.2025.104739
Received 20 December 2024; Received in revised form 25 February 2025; Accepted 25 February 2025
Available online 4 March 2025

reduction—through bacterial sulfate reduction (BSR) or thermochemical sulfate reduction (TSR)—or by providing reduced sulfur for mineralization (Jochum, 2000; Xiong et al., 2019). Kesler et al. (1994) reported that the sulfides and oil in Mississippi Valley-type (MVT) Pb—Zn deposits along the Cincinnati Arch shared nearly identical $\delta^{34}S_{CDT}$ values (−9 ‰ to +9 ‰ for MVT Pb—Zn deposit sulfides; −12 ‰ to +9 ‰ for oils).

The genetic linkage between the formation of solid bitumen and the mineralization process has not been thoroughly studied. Comprehensive research on the genetic relationship between ore deposit geology and petroleum geology remains limited (Gu et al., 2010). A key question persists: does mineralization influence hydrocarbon accumulation, or does hydrocarbon accumulation drive metal mineralization? This study combined ore deposit geology and petroleum geology to investigate the connection between mineralization and hydrocarbon accumulation or destruction. Outcrop observations of ores and solid bitumen, along with reflected light microscopy and scanning electron microscopy (SEM), were conducted to examine mineralogical features and reconstruct the precipitation sequences of ore minerals and solid bitumen in reservoirs. To assess the impact of metallogenesis on hydrocarbons, bitumen reflectance and the elemental composition of solid bitumen, both coexisting with minerals and occurring independently, were measured and compared. Additionally, the homogenization temperatures of fluid inclusions in ore-stage calcite were analyzed. Sulfur isotopic compositions of sulfide ores were examined to identify potential sulfur sources and infer hydrocarbon maturity. The ore-forming process was found to enhance the thermal maturity of organic matter, influencing hydrocarbon reconstruction or destruction. Organic matter played a crucial role in reducing sulfur for metallogenesis, as demonstrated by sulfur isotope analysis.

2. Geological setting

Southwest China encompasses several major geological units, including the Xuefeng Mountains Uplift, Central Guizhou Uplift, Nanpanjiang Basin, Longmen Shan Orogenic Belt, Micang-Daba Mountains Uplift, Kangdian Axis, Sichuan Basin, and Lanpin–Simao Basin (Fig. 1). The geological setting of Southwest China was previously described by He et al. (2011). Briefly, the evolution of this region can be divided into three stages: (i) formation and development of the Yangtze ancient landmass; (ii) evolution of stable cratonic basins from the Sinian to the Middle Triassic; and (iii) formation of inland lake basins since the Late Triassic. The dynamic evolution of this area is broadly marked by the Triassic, characterized by alternating extensional and compressional phases during the earlier period and compressional features in the later period, resulting in the orderly superposition of multiple basins (Li et al., 2015; Zhang et al., 2007).

The stratigraphic deposition in the study area consisted of a Precambrian basement composed of Banxi Group metamorphic and igneous rocks, overlain by Sinian to Middle Triassic strata dominated by marine carbonates, and Upper Triassic to Quaternary strata characterized by terrestrial clastic rocks (Fig. 2) (Wei et al., 2020). This study focused on pre-Jurassic carbonate rocks containing bitumen and low- to medium-temperature hydrothermal minerals. Potential source rocks for solid

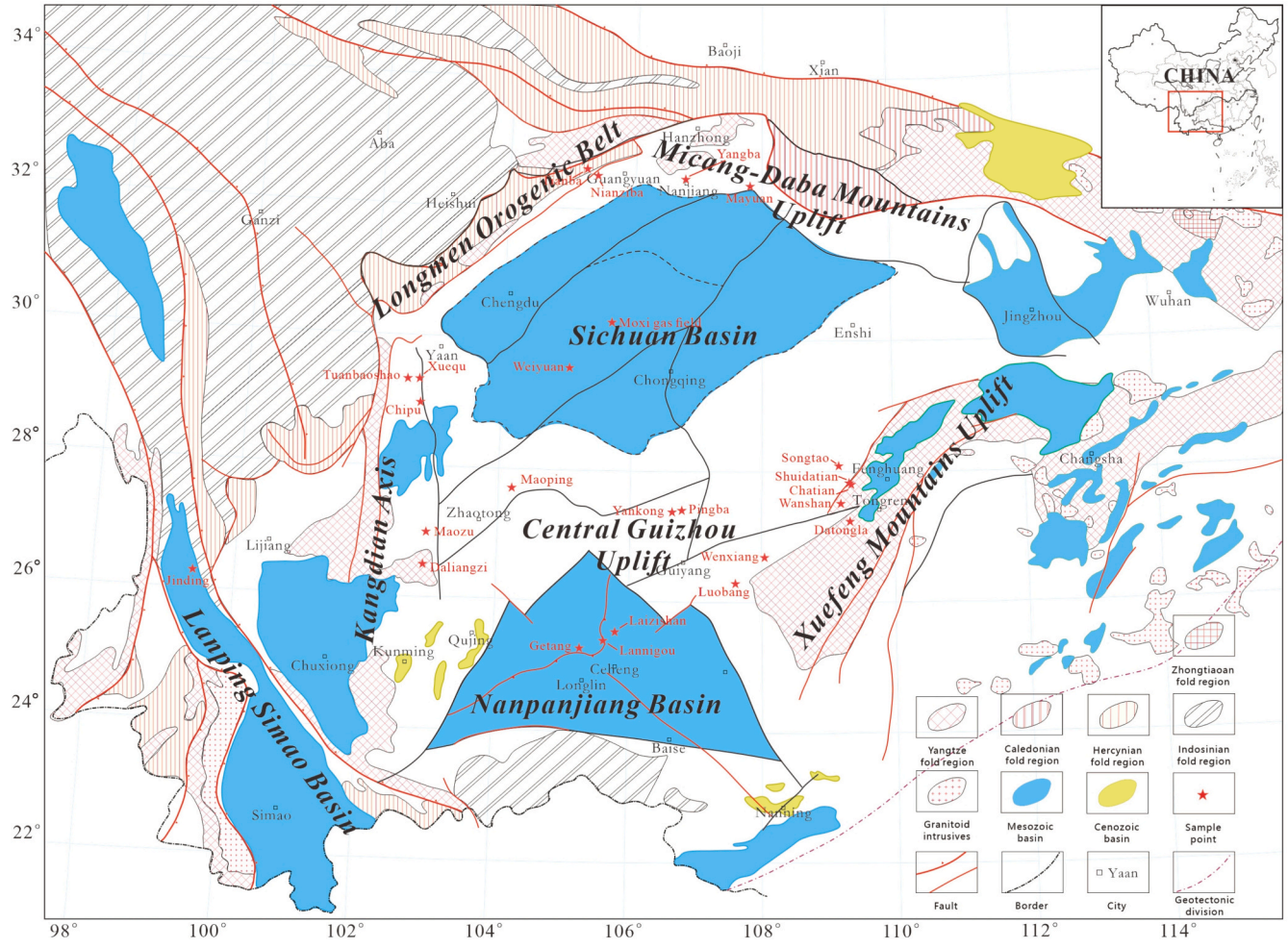

Fig. 1. Tectonic schematic and distribution of solid bitumen in Southwest China.

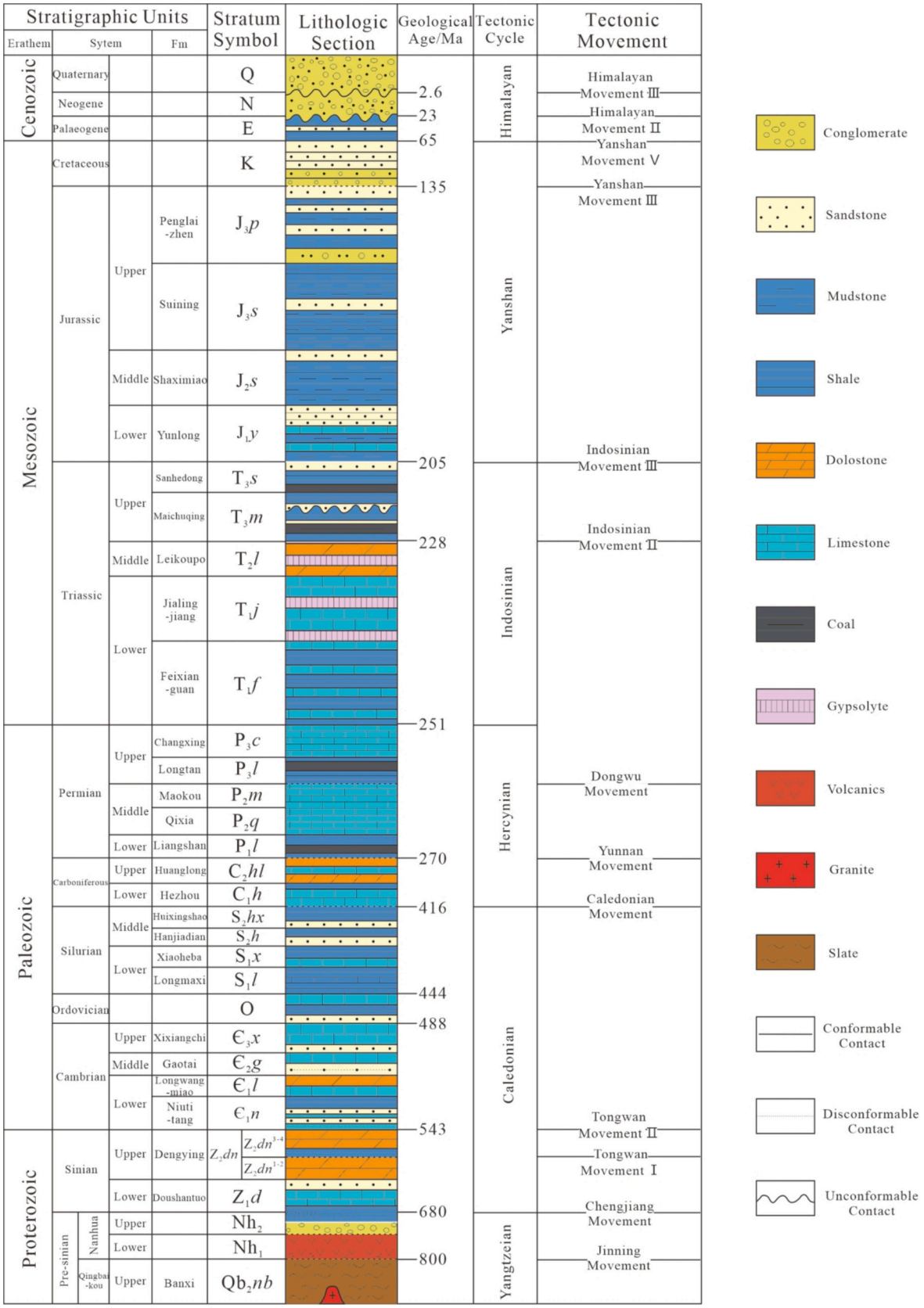

Fig. 2. Simplified stratigraphic column of Southwest China (Sinian system equals to Ediacaran system according to the IUGS International Chronostratigraphic column).

bitumen included the micrites of the Doushantuo Formation (Z_1d), micrites and shale of the Dengying Formation (Z_2dn), mudstone and shale of the Niutitang Formation ($\in_1n$), shale of the Longtan Formation (P_3l), and mudstone and shale of the Maichuqing Formation (T_3m).

3. Samples and experiments

3.1. Samples

A total of 25 solid bitumen samples, 2 cinnabar samples, 8 lead-zinc ore samples, and 2 disseminated gold samples were collected from freshly exposed outcrops in Southwest China to ensure that they remained uncontaminated and unoxidized (Table 1), following the standard ISO 7404-5 (2009). Sampling localities are documented in Fig. 1. Most solid bitumen samples were obtained from Cambrian and Sinian carbonate reservoirs, which also served as the surrounding rocks of the deposits. Samples from the Nanpanjiang Basin and Lanping-Simao Basin were collected from the Permian and Triassic strata. The solid bitumen samples exhibit the characteristics of the pyrobitumen as defined by Sanei (2020), which are believed to be closely linked to the formation, reconstruction and destruction process of paleo-oil reservoirs. The associations between these organic matter and minerals were summarized based on the deposit type (Table 1).

3.2. Microscopy

A Leica DM4500P reflected light microscope equipped with a CRAIC microscope photometer was used for observation and reflectance measuring. Each sample had around 30 measurement points for the reflectance of solid bitumen values (%BRo). Under polarized light conditions, the microscope stage was rotated through a full 360° to determine the highest and lowest apparent reflectance values (%BRomax and %BRomin) at each point. Detailed description of the measurement is available in Yao et al. (2021). The optical textures of the solid bitumen, observed under cross-polarized light, were categorized according to the classifications proposed by Grint and Marsh (1981). The measurement follows ISO 7404-5 (2009).

3.3. Scanning electron microscopy (SEM)

A microscopic examination was conducted using an FEI Quanta 200F SEM instrument fitted with an energy-dispersive X-ray spectrometry (EDS) system. Imaging was carried out under vacuum conditions at an acceleration voltage of 20 kV and a working distance of approximately 10.0 mm. The elemental weight and atomic percentages were corrected using the EDAX-ZAF standardization method.

3.4. Rock pyrolysis

Prior to the rock and element analysis, the outcrop samples containing solid bitumen needed to be crushed and clean. The pure solid bitumen samples were selected under a microscope (10× magnification). Detailed description of the measuring procedures is available in Yao et al. (2021).

Table 1
Location and occurrence of typical solid bitumen in Southwest China.

Tectonic unit	Sample ID	Location	Latitude	Longitude	Age*	Occurrence
Sichuan Basin	MX-SB-1	Moxi gas field, Sichuan	30°16′40″	105°40′32″	$\in_1$	only SB
	WY-SB-2	Weiyuan, Sichuan	29°34′41″	105°1′5″	Z_2dn	only SB
Longmen Orogenic Belt	TB-SB-1	Tianba, Guangyuan, Sichuan	32°28′27″	105°24′54″	$\in_1$	only SB
	KSL-SB-1	Nianziba, Guangyuan, Sichuan	32°19′9″	105°22′57″	$\in_1$	only SB
	KSL-Ca-1	Nianziba, Guangyuan, Sichuan	32°19′9″	105°22′57″	$\in_1$	calcite veins associated with KSL-SB-1
	YB-SB-3	Yangba, Nanzheng, Shanxi	32°27′59″	106°47′32″	$\in_1$	only SB
	YB-Ca-4	Yangba, Nanzheng, Shanxi	32°27′59″	106°47′32″	$\in_1$	calcite veins associated with YB-SB-3
Micang-Daba Mountains Uplift	MY-SB-2	Mayuan, Nanzheng, Shanxi	32°21′31″	107°48′24″	Z_2dn	SB in MVT deposits
	MY-sp-2	Mayuan, Nanzheng, Shanxi	32°21′31″	107°48′24″	Z_2dn	sphalerite separated from MY-SB-2
	MY-ga-2	Mayuan, Nanzheng, Shanxi	32°21′31″	107°48′24″	Z_2dn	galena separated from MY-SB-2
Xuefeng Mountains Uplift	WS-SB-1	Wanshan, Tongren, Guizhou	27°30′43″	109°12′54″	$\in_3$	SB in stratiform mercury deposits
	DGL-SB-2	Shuidatian, Fenghuang, Guizhou	27°50′58″	109°37′6″	$\in_3$	SB in MVT deposits
	DGL-Ca-3	Shuidatian, Fenghuang, Guizhou	27°50′58″	109°37′6″	$\in_3$	calcite veins associated with DGL-SB-2
	DGL-sp-2	Shuidatian, Fenghuang, Guizhou	27°50′58″	109°37′6″	$\in_3$	sphalerite separated from DGL-SB-2
Central Guizhou Uplift	CT-SB-1	Chatian, Fenghuang, Guizhou	27°48′55″	109°21′30″	$\in_1$	SB in stratiform mercury deposits
	ST-SB-3	Songtao, Guizhou	28°5′2″	109°10′52″	$\in_1$	only SB
	DZ-SB-3	Datongla, Tongren, Guizhou	27°45′55″	109°21′4″	$\in_{2\text{-}3}$	only SB
	YK-SB-1	Yankong, Jinsha, Guizhou	27°21′41″	106°38′16″	Z_2dn	only SB
	PB-SB-2	Pingba, Jinsha, Guizhou	27°22′02″	106°38′43″	Z_2dn	only SB
	LB-SB-1	Luobang, Duyun, Guizhou	26°16′26″	107°35′32″	P_1	only SB
	MJ-SB-2	Wengxiang, Kaili, Guizhou	26°40′17″	108°1′54″	S_1	only SB
	GT-SB-1	Getang, Anlong, Guizhou	25°17′7″	105°18′27″	P_2	only SB
	GT-Ca-2	Getang, Anlong, Guizhou	25°17′7″	105°18′27″	P_2	calcite veins associated with GT-SB-1
Nanpanjiang Basin	CH-SB-4	Laizishan, Ceheng, Guizhou	25°4′7″	105°49′5″	P_1	SB in disseminated gold deposits
	ZF-SB-2	Lannigou, Zhenfeng, Guizhou	25°24′8″	105°39′24″	T_1	SB in disseminated gold deposits
	ZF-Ca-3	Lannigou, Zhenfeng, Guizhou	25°24′8″	105°39′24″	T_1	calcite veins associated with ZF-SB-2
	ZF-py-2	Lannigou, Zhenfeng, Guizhou	25°24′8″	105°39′24″	T_1	pyrite separated from ZF-SB-2
	TBS-SB-1	Tuanbaoshan, Hanyuan, Sichuan	29°21′40″	102°38′18″	$\in_1$	SB in MVT deposits
	TBS-Ca-2	Tuanbaoshan, Hanyuan, Sichuan	29°21′40″	102°38′18″	$\in_1$	calcite veins associated with TBS-SB-1
Kangdian Axis	MP-SB-1	Maoping, Yiliang, Yunnan	27°39′3″	104°6′47″	Z_2dn	SB in MVT deposits
	XQ-SB-2	Xuequ, Hanyuan, Sichuan	29°21′31″	102°48′24″	Z_2dn	SB in MVT deposits
	XQ-Ca-3	Xuequ, Hanyuan, Sichuan	29°21′31″	102°48′24″	Z_2dn	calcite veins associated with XQ-SB-2
	CP-SB-3	Chipu, Ganluo, Sichuan	28°59′22″	102°49′1″	Z_2dn	SB in MVT deposits
	HD-SB-1	Daliangzi, Liangshan, Sichuan	26°27′47″	102°50′36″	Z_2dn	only SB
	MZ-SB-2	Maozu, Zhaotong, Yunnan	26°57′58″	102°53′33″	Z_2dn	SB in MVT deposits
	MZ-Ca-3	Maozu, Zhaotong, Yunnan	26°57′58″	102°53′33″	Z_2dn	calcite veins associated with MZ-SB-2
	MZ-sp-2	Maozu, Zhaotong, Yunnan	26°57′58″	102°53′33″	Z_2dn	sphalerite separated from MZ-SB-2
	MZ-ga-2	Maozu, Zhaotong, Yunnan	26°57′58″	102°53′33″	Z_2dn	galena separated from MZ-SB-2
Lanping-Simao Basin	LP-SB-3	Jinding, Lanping, Yunna	26°14′36″	99°13′48″	T_3	SB in MVT deposits
	LP-sp-3	Jinding, Lanping, Yunna	26°14′36″	99°13′48″	T_3	sphalerite separated from LP-SB-3

* The age symbols are shown in Fig. 2.

To determine Tmax, S1, and S2, analyses were performed using the Leco CS230 and HAWK pyrolysis system (Espitalié et al., 1977), which is equivalent to regular Rock-Eval analysis (Luo et al., 2021). In the HAWK pyrolysis process, samples underwent pyrolysis at 300 °C for 3 min, followed by heating at a rate of 25 °C per minute until reaching 650 °C. The quantities of released hydrocarbons, designated as S1 and S2, were measured using a flame ionization detector (FID). The accuracy and precision of S1 and S2 measurements exceeded 5 %, while Tmax accuracy was maintained within ±2 °C. These performance metrics were validated through the analysis of standard reference materials, specifically: (i) WT2 from Wildcat Technologies (USA), and (ii) Chinese standard reference materials.

3.5. Element and sulfur isotope analysis

The organic elemental composition of solid bitumen was analyzed using an elemental analyzer (Vario EL cube). The hand-picked, pure solid bitumen sample was crushed to a 60-mesh size (approximately 1.2 mm) and examined under a stereo-microscope at 100× magnification to confirm the absence of metal minerals such as pyrite in the particles prior to its use for organic elemental analysis. The analysis of element is based on the method Yang et al. (2018),following the standard ASTM D5291–21.

Sulfur isotope analysis was performed utilizing a Nu Plasma II MC-ICP-MS, which was equipped with a Resonetics-S155 excimer ArF laser ablation system. For the experimental setup, the laser beam diameter was configured to 33 μm, operating at a frequency of 10 Hz, and each ablation event continued for 40 s. To ascertain the $\delta^{34}S$ values of the samples during the MC-ICP-MS sessions, the standard-sample bracketing (SSB) method was employed (Craddock et al., 2008). The accurate sulfur isotope ratios were derived by correcting for instrumental mass bias through linear interpolation based on biases from adjacent standard analyses. Isotopic results are expressed in delta notation (‰), relative to the Vienna Canyon Diablo Troilite (CDT) standard:

$$\delta^{34}S_{CDT} = \left[\left(\left({}^{34}S/{}^{32}S\right)_{sample} \Big/ \left({}^{34}S/{}^{32}S\right)_{CDT}\right) - 1\right] \times 10^3$$

The $({}^{34}S/{}^{32}S)_{sample}$ represents the measured $^{34}S/^{32}S$ ratio within the sample, while $({}^{34}S/{}^{32}S)_{CDT}$ is established as 0.04416 (Ding et al., 2001). The analytical precision 2σ was estimated to be: ±0.2 per mil.

These experiments were conducted at the state Key Laboratory of Petroleum Resources and Engineering at the China University of Petroleum except the sulfur isotope analyses were carried out at the Laboratory for Stable Isotope Geochemistry, Institute of Geology and Geophysics, Chinese Academy of Sciences.

4. Results and Discussion

4.1. Occurrences of associations between solid bitumen and low- to medium-temperature hydrothermal minerals

4.1.1. MVT deposits and their associations with solid bitumen

MVT deposits are lead–zinc deposits associated with basin brine, with carbonate rock serving as the host rock (Leach et al., 2001). The association between organic matter and minerals varied significantly due to the thermal maturity of the organic matter. Based on the thermal maturity of solid bitumen associated with sulfide minerals, the association patterns were divided into two types:

4.1.1.1. Low organic thermal maturity type. The Jinding superlarge lead–zinc deposit in the Lanping–Simao Basin is a typical example of the low organic thermal maturity type (Sample LP-SB-3). The primary ore-hosting horizon was the Upper Triassic Sanhedong Formation (T_3s), which also contained the reservoir of the Lanping paleo-oil field. The organic matter in the deposit exhibited low maturity, with solid bitumen showing low reflectivity under reflected light (BRo = 0.67 %, Table 2). In a few cases, solid bitumen occurs alone in calcite veins (Fig. 3A); in most cases, it associated with lead–zinc minerals (Fig. 3B).

4.1.1.2. High and over thermal maturity type. Most organic matter in MVT deposits in Southwest China is pyrobitumen (Fig. 3C, D, E, F, G, H), which shows high reflectivity under reflected light (BRo >2.0 %, Table 2). Sample DGL-SB-2, collected from the Xixiangchi Formation ($\in_3x$) in the Xuefeng Mountains Uplift, was solid bitumen associated with sphalerite (Fig. 3C). Under reflected light, the solid bitumen exhibited strong optical anisotropy with fine-grained mosaic and coarse-grained mosaic textures (Fig. 4A). SEM analysis showed that the solid bitumen surrounded and encapsulated sphalerite (ZnS) particles (Fig. 5A), indicating that the minerals formed slightly earlier than the solid bitumen. Sample XQ-SB-2, collected from the Dengying Formation (Z_2dn) in the Kangdian Axis, was solid bitumen associated with sphalerite within dissolution pores (Fig. 3D). Under reflected light, the solid bitumen exhibited strong optical anisotropy with fine-grained mosaic, coarse flow mosaic and domain textures (Fig. 4B). SEM analysis revealed that sphalerite and barite ($BaSO_4$) encapsulated solid bitumen (Figs. 5B, 6A, B), indicating that the solid bitumen formed slightly earlier than the minerals. Similarly, sample MZ-SB-2, MY-SB-2 and TBS-SB-1 show the solid bitumen associated with lead–zinc minerals by directly surrounding the mineral particles (Figs. 5C, D, 6C, D) or occurring within them (Fig. 5E). These observations suggest that most solid bitumen in MVT deposits in Southwest China is pyrobitumen, which displays complex textures (Gentzis and Goodarzi, 1990).

4.1.2. Stratiform mercury deposits and their associations with solid bitumen

In Southwest China, stratiform mercury deposits primarily occur in the Xuefeng Mountains Uplift and are typically integrated and layered or nearly layered. The ore-hosting strata consist of Cambrian lower Longwangmiao Formation dolostone ($\in_1l$) and Xixiangchi limestone ($\in_3x$). Sample CT-SB-1, collected from the Longwangmiao Formation ($\in_1l$), revealed that cinnabar particles were encapsulated by solid bitumen in dissolution and intercrystal pores (Fig. 3E). Solid bitumen was also observed as dispersed small pieces within rhombohedral cinnabar particles (Fig. 4E), indicating that the solid bitumen formed earlier than the cinnabar. SEM analysis revealed that HgS is distributed in FeS fractures (Figs. 5F, 6D, E).

4.1.3. Disseminated gold deposits and their associations with solid bitumen

Disseminated gold deposits, also referred to as Carlin-type or Carlin-like gold deposits, were primarily distributed in the Nanpanjiang Basin. The ore-bearing strata mainly consisted of Permian bioclastic limestone, which also contained the Zhenfeng and Lannigou paleo-oil reservoirs. Gold occurred in two forms: as fine particles in arsenian pyrite or as disseminations in solid bitumen. Arsenian pyrite frequently cooccurred with solid bitumen (Figs. 3F, 4F), indicating a significant relationship between the ore-forming process and organic matter (Sample ZF-SB-2). Micron-scale gold particles were observed in the solid bitumen via SEM (Fig. 7). Although the SEM signal was influenced by surrounding minerals, gold could still be identified (Fig. 7). This indicates that gold migration was associated with petroleum; when petroleum formed solid bitumen, gold precipitated.

4.1.4. Solid bitumen without the associated metal minerals

For comparison, two types of solid bitumen not associated with deposits were also collected. The first type consisted of solid bitumen from a paleo-oil reservoir near the deposits. Sample YB-SB-3, collected from the Dengying Formation (Z_2dn) in the Micang-Daba Mountains Uplift, represented solid bitumen within a stylolite (Fig. 3G). Under reflected light, the solid bitumen exhibited strong optical anisotropy (Fig. 4G). SEM analysis identified a small PbS particle within the solid bitumen (Fig. 5G), indicating that the paleo-oil reservoir was influenced by

Table 2
Measured reflectance and equivalent vitrinite reflectance of solid bitumen from Southwest China.

Sample ID	Age*	Rock pyrolysis			Bitumen reflectance				EqVRo (%)**
		Tmax (°C)	S1 (mg/g)	S2 (mg/g)	BRo (%)	BRomax (%)	BRomin (%)	ΔBRo (%)	
MX-SB-1	$\in_1$	/	BRL***	BRL	2.59	4.92	0.79	4.13	2.00
WY-SB-2	Z_2dn	/	BRL	BRL	3.35	4.77	1.19	3.58	2.47
TB-SB-1	$\in_1$	/	BRL	BRL	0.24	0.45	0.15	0.30	0.55
YB-SB-3	$\in_1$	/	BRL	BRL	3.27	5.36	2.04	3.32	2.42
MY-SB-2	Z_2dn	/	BRL	BRL	4.46	8.44	0.54	7.90	3.16
WS-SB-1	$\in_3$	/	BRL	BRL	3.10	5.03	0.75	4.28	2.32
DGL-SB-2	$\in_3$	/	BRL	BRL	3.23	4.97	0.71	4.26	2.39
CT-SB-1	$\in_1$	/	BRL	BRL	3.45	4.23	0.91	3.32	2.53
ST-SB-3	$\in_1$	/	BRL	BRL	4.16	4.48	3.68	0.80	2.97
DZ-SB-3	$\in_{2-3}$	/	BRL	BRL	2.52	3.11	1.14	1.97	1.96
YK-SB-1	Z_2dn	/	BRL	BRL	4.48	7.36	1.66	5.70	3.17
PB-SB-2	Z_2dn	/	BRL	BRL	5.04	7.81	0.57	7.24	3.51
LB-SB-1	P_1	545	0.13	2.15	1.78	2.84	1.20	1.64	1.50
MJ-SB-2	S_1	486	0.16	2.47	1.52	2.42	0.71	1.71	1.34
GT-SB-1	P_2	/	BRL	BRL	3.40	4.24	2.82	1.42	2.50
CH-SB-4	P_1	/	BRL	BRL	3.85	4.92	0.96	3.96	2.78
ZF-SB-2	T_1	/	BRL	BRL	3.47	5.22	0.47	4.75	2.55
TBS-SB-1	$\in_1$	/	BRL	BRL	4.00	5.21	0.55	4.66	2.87
MP-SB-1	Z_2dn	/	BRL	BRL	3.84	6.26	0.65	5.61	2.77
XQ-SB-2	Z_2dn	/	BRL	BRL	4.95	8.14	0.37	7.77	3.46
CP-SB-3	Z_2dn	/	BRL	BRL	5.17	6.00	0.87	5.13	3.60
HD-SB-1	Z_2dn	/	BRL	BRL	2.67	3.41	1.81	1.60	2.05
MZ-SB-2	Z_2dn	/	BRL	BRL	4.98	10.14	0.33	9.81	3.48
LP-SB-3	T_3s	441	0.05	0.59	0.67	0.73	0.62	0.11	0.81

**EqVRo calculated via Jacob (1989): EqVRo% = 0.618*BRo% + 0.4 (BRo means bitumen reflectance; EqVRo means equivalent vitrinite reflectance) (Jacob, 1989).
* The age symbols are shown in Fig. 2.
*** BRL means below reporting limits.

metallogenetic processes. The ore-forming brines containing Pb likely entered the paleo-oil reservoir and facilitated material exchange.

The other type consisted of solid bitumen not associated with metallogenetic processes. Sample ST-SB-3, collected from the Niutitang Formation ($\in_1$n) in the Xuefeng Mountains Uplift, represented in-source secondary solid bitumen within a calcite vein (Fig. 3H). Detailed information can be found in the literature Yao et al. (2021). Under reflected light, the solid bitumen appeared homogeneous, which differed from solid bitumen influenced by mineralization (Fig. 4H). SEM analysis revealed numerous small pores on the surface of the solid bitumen, attributed to shrinkage during thermal maturation (Fig. 5H).

4.2. Petrological characteristics of the solid bitumen

As a product of hydrocarbon alteration, the petrological characteristics of solid bitumen provide insights into the evolution of hydrocarbons. Notably, the petrological features of solid bitumen associated with minerals suggest the influence of mineralization on hydrocarbons. By analyzing and comparing the elemental compositions of mineral-associated solid bitumen with those of non-mineral-associated samples, we demonstrated how ore-forming processes impacted the elemental composition of hydrocarbons.

4.2.1. Organic petrological characteristics of the solid bitumen

Source rocks in ancient marine strata often lack vitrinites, making it impossible to measure vitrinite reflectance directly. In this situation, solid bitumen reflectance is one of the parameters still available for assessing hydrocarbon maturity. A petrographic analysis was conducted on the extensive solid bitumen found in reservoirs within the study area (Table 2).

In Southwest China, the solid bitumen in reservoirs—particularly within the Sinian-Cambrian strata—contains negligible residual hydrocarbons (S1) and pyrolytic hydrocarbons (S2), which caused pyrograms below reporting limits, rendering Tmax measurements unreliable (Peters, 1986). Carrie et al. (2012) believed that that any S2 values below 0.2 mg/g are unreliable, which indicates the solid bitumen is in high-overmature thermal stage. The reflectance of solid bitumen ranged from 0.24 % to 5.17 %, indicating significant variations in maturity across different regions and strata. Most solid bitumen exhibited a reflectance exceeding 2.5 %, while the equivalent vitrinite reflectance (EqVRo) was over 2.0 %, indicating that the solid bitumen was in a postmature stage. The difference between BRomax and BRomin represents the anisotropy of solid bitumen. Solid bitumen associated with sulfide minerals exhibited stronger anisotropy (ΔBRo >3.32 %) (Fig. 8). All solid bitumen associated with minerals was located in Region A (Fig. 8), indicating that these solid bitumen were likely affected by abnormal heat during their formation (Goodarzi et al., 1993). These heat sources are likely connected to ore-forming processes.

4.2.2. Organic elemental composition of solid bitumen

Solid bitumen primarily consists of organic elements, including carbon (C), hydrogen (H), oxygen (O), nitrogen (N), and sulfur (S). The organic elemental composition of solid bitumen varies depending on the original hydrocarbon source. We analyzed the organic elemental composition of 20 solid bitumen samples (Table 3).

Most samples exhibited H/C ratios ranging from 0.286 to 0.490 and O/C ratios ranging from 0.016 to 0.113, indicating a high maturity of the solid bitumen. The S/C ratio of solid bitumen associated with mineralization ranged from 0.029 to 0.033, while that of nonmineralized samples ranged from 0.005 to 0.021. Thus, solid bitumen associated with metal minerals exhibited a higher S/C ratio.

4.3. Metallogenic characteristics of low- to medium-temperature hydrothermal mineral deposits

Numerous low- to medium-temperature hydrothermal mineral deposits were distributed in Southwest China, with their metallogenic characteristics reflecting the ore-forming processes involved. In this study, we compiled metallogenic ages from existing research and identified statistical patterns across different regions. Metallogenic temperatures were determined by measuring the homogenization temperature of fluid inclusions, while sulfur sources were inferred from the sulfur

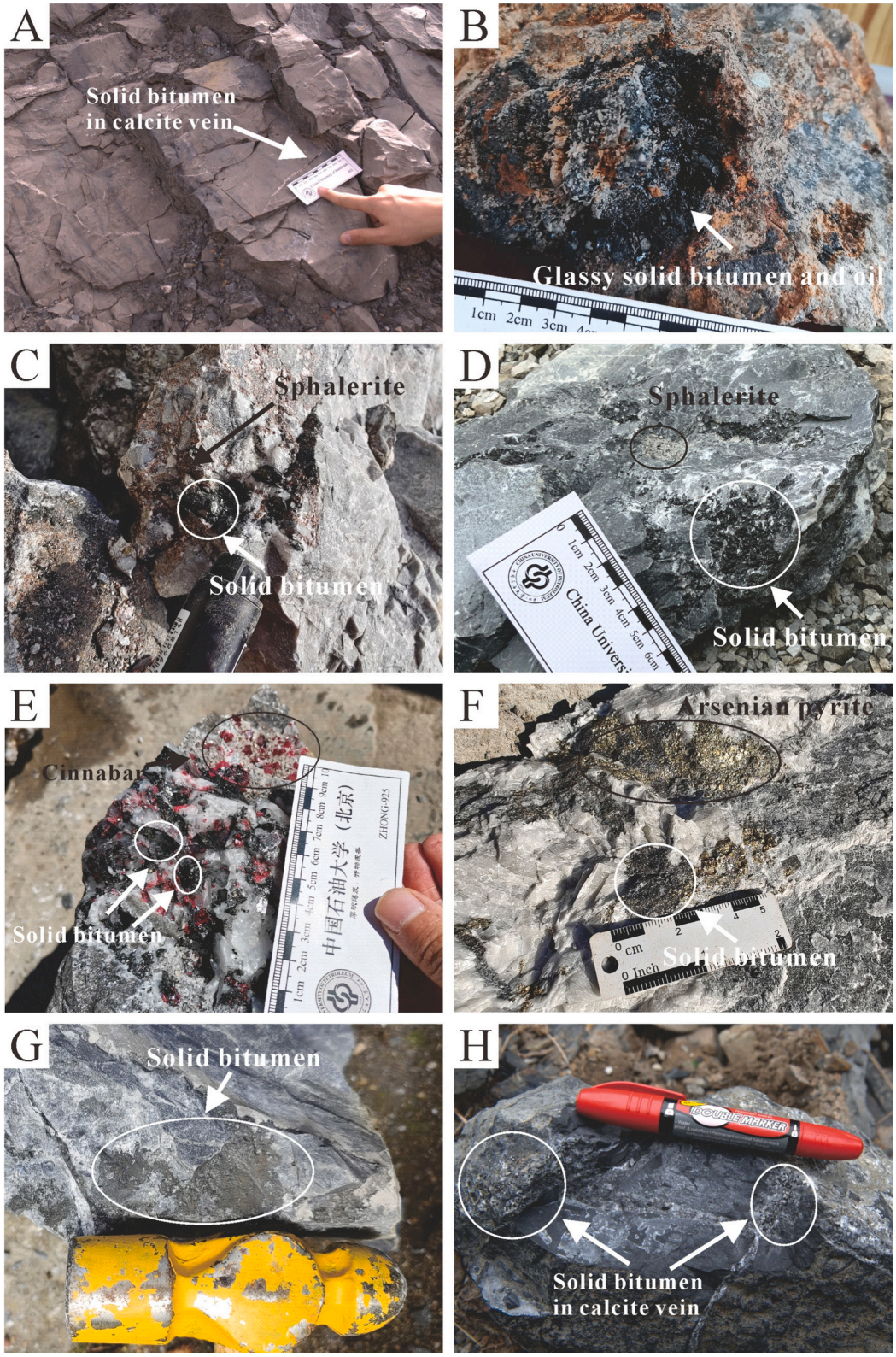

Fig. 3. Photographs showing the occurrence of solid bitumen: (A) Solid bitumen in calcite vein in MVT deposits from the Lanping-Simao Basin; (B) Glassy solid bitumen and oil associated with sphalerite in MVT deposits from the Lanping-Simao Basin; (C) Solid bitumen associated with sphalerite in MVT deposits from the Xuefeng Mountain Uplift (DGL-SB-2); (D) Solid bitumen associated with sphalerite in MVT deposits from the Kangdian Axis (XQ-SB-2); (E) Solid bitumen associated with cinnabar in stratiform mercury deposits from the Xuefeng Mountain Uplift (CT-SB-1); (F) Solid bitumen associated with arsenian pyrite from disseminated gold deposits in the Nanpanjiang Basin (ZF-SB-2); (G) Solid bitumen in a stylolite from a paleo-oil reservoir near the deposits in the Micang-Daba Mountain Uplift (YB-SB-3); (H) Solid bitumen in calcite vein not associated with mineralization from the Xuefeng Mountain Uplift (ST-SB-3). (For interpretation of the references to colour in this figure legend, the reader is referred to the web version of this article.)

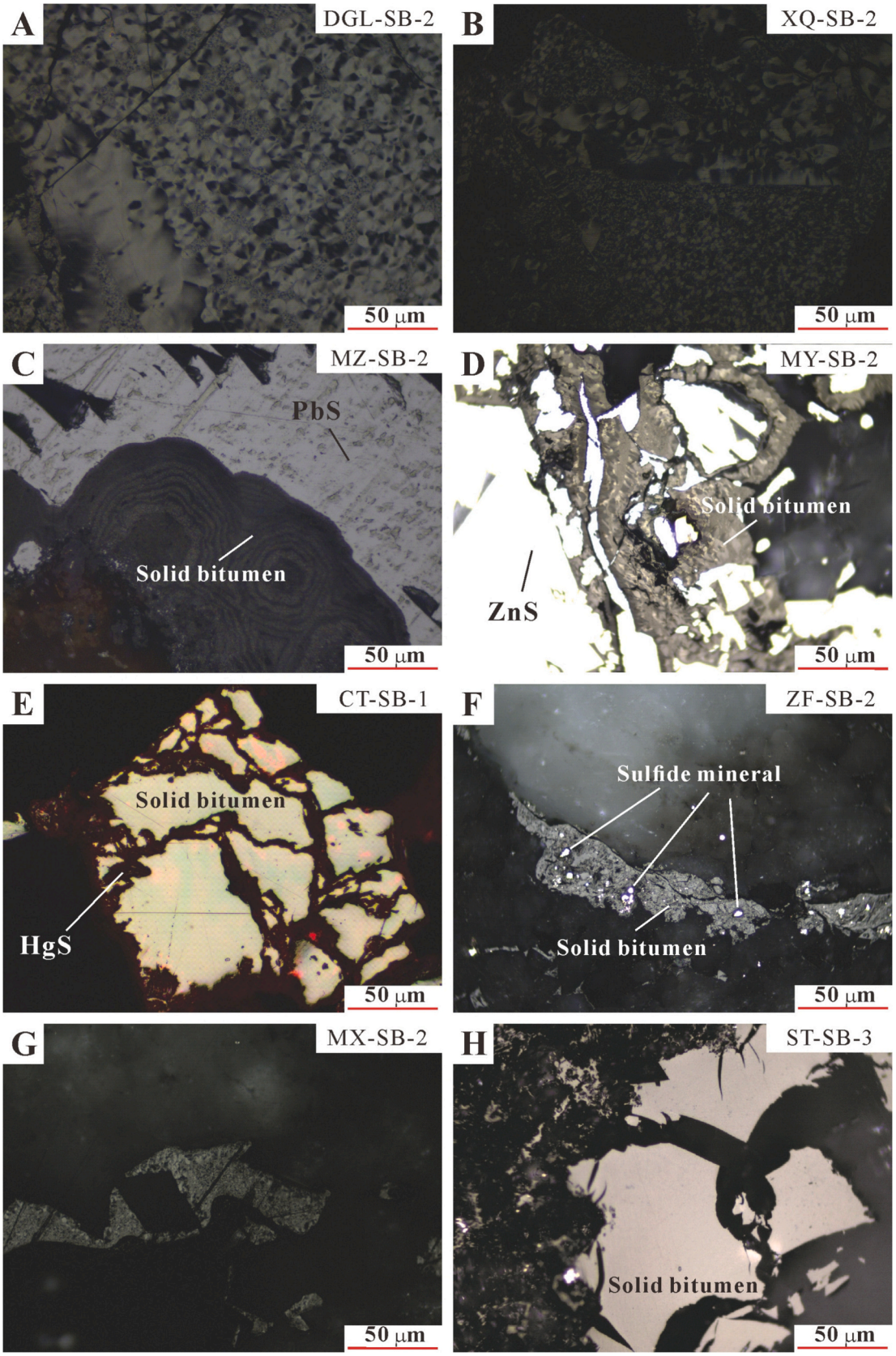

Fig. 4. Photographs under microscope showing petrographic characteristics of solid bitumen: (A) solid bitumen with strong optical anisotropy. Oil-immersion, polarized light; (B) solid bitumen with strong optical anisotropy. Oil-immersion, polarized light; (C) solid bitumen associated with galena (PbS). Oil-immersion, polarized light; (D) solid bitumen associated with sphalerite (ZnS). Oil-immersion, polarized light; (E) solid bitumen surrounded by cinnabar. Oil-immersion, reflected light; (F) solid bitumen associated with sulfide mineral. Oil-immersion, polarized light; (G) solid bitumen with strong optical anisotropy. Oil-immersion, polarized light; (H) solid bitumen with homogeneous texture. Oil-immersion, polarized light.

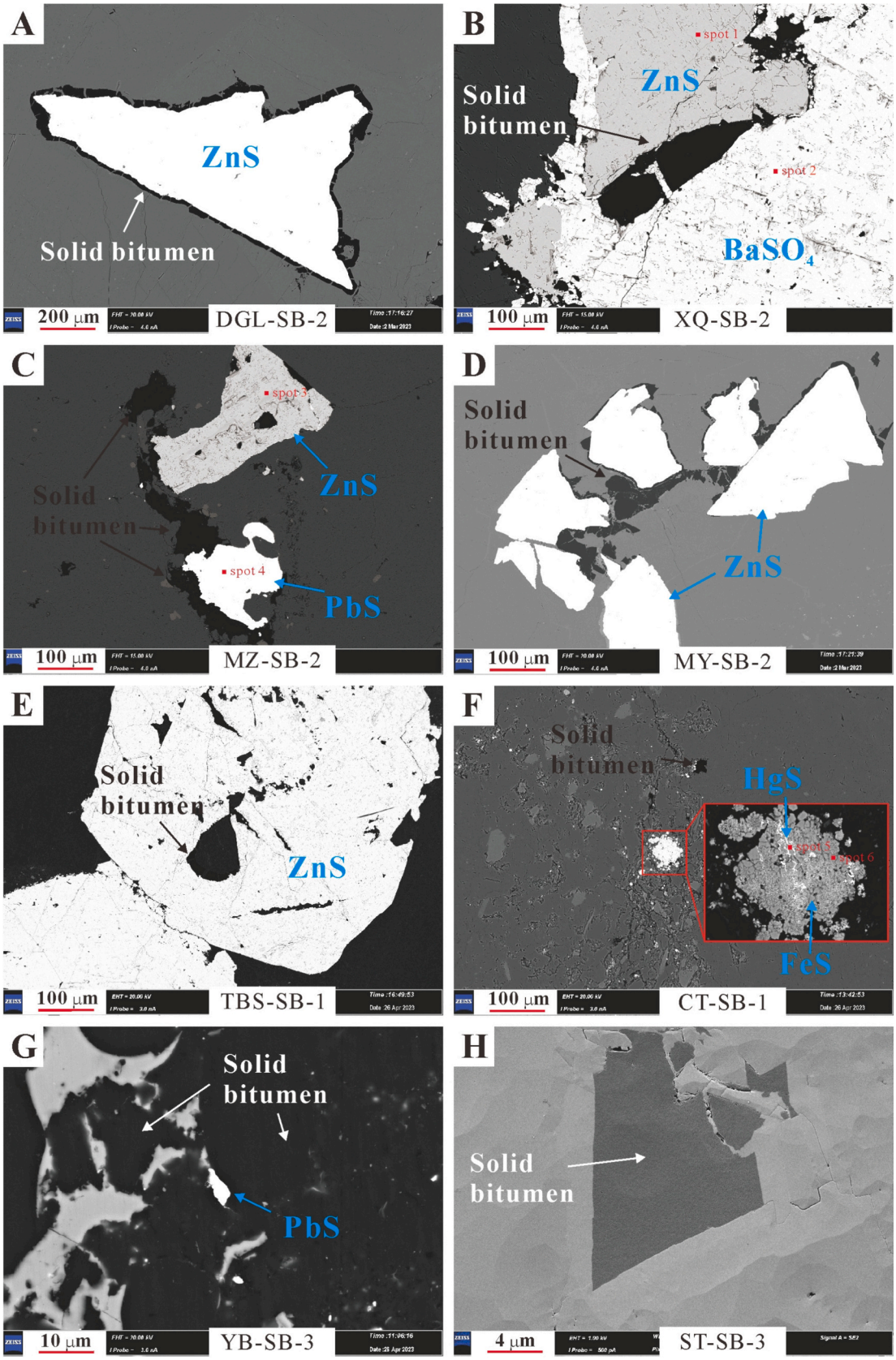

Fig. 5. Photographs under scanning electron microscope (SEM): (A) solid bitumen associated with ZnS particle; (B) solid bitumen associated with ZnS-$BaSO_4$, energy-dispersive spectroscopy (EDS) of spot 1 and 2 in Fig. 6A, B; (C) solid bitumen associated with ZnS-PbS, EDS of spot 3 and 4 in Fig. 6C, D; (D) solid bitumen associated with ZnS particle; (E) solid bitumen associated with ZnS particle; (F) solid bitumen associated with HgS-FeS, EDS of spot 5 and 6 in Fig. 6E, F; (G) solid bitumen associated with small PbS particle; (H) Solid bitumen not associated with mineralization.

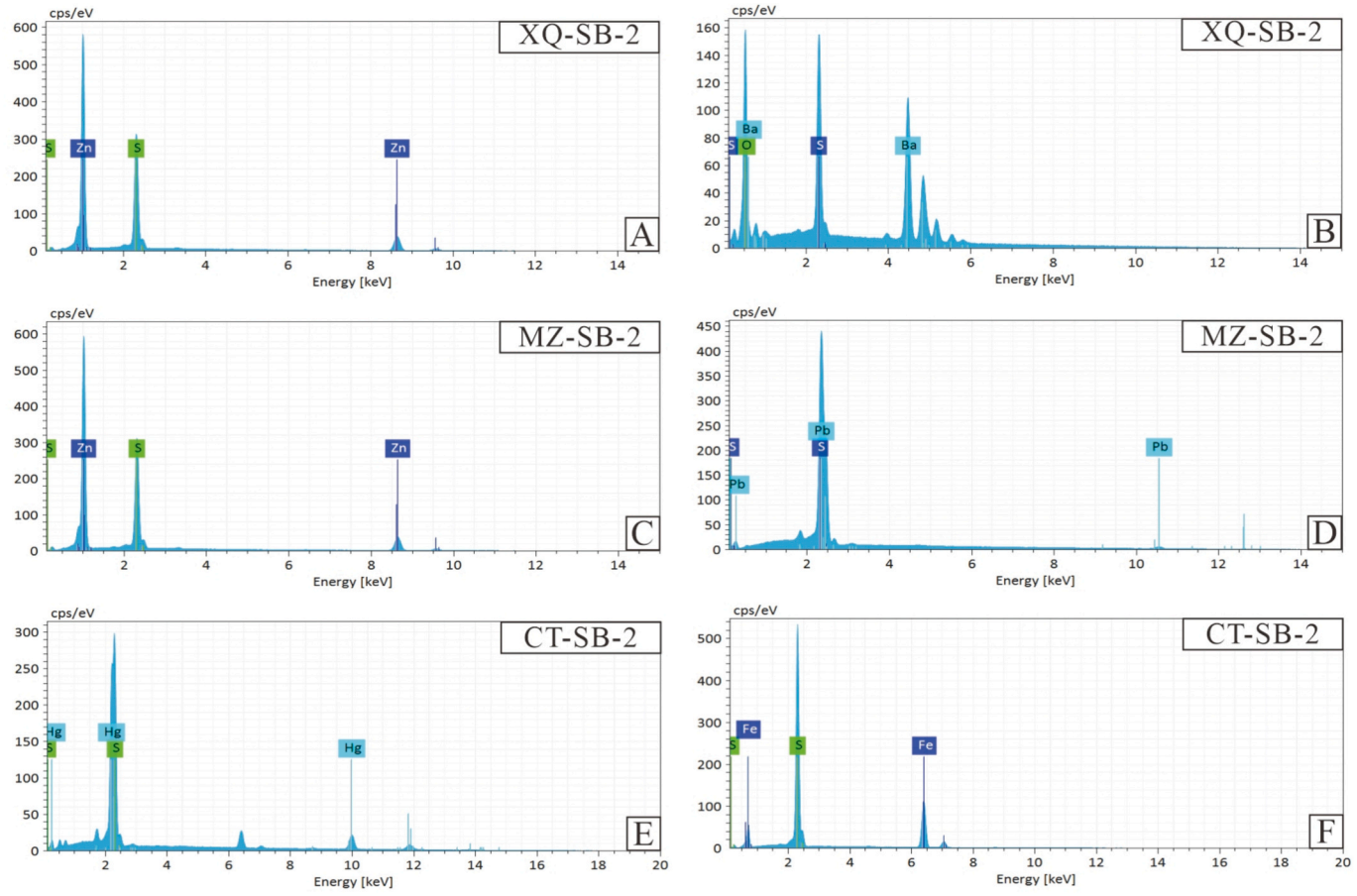

Fig. 6. Energy-dispersive spectroscopy (EDS) spectra of mineral particles: (A) ZnS in sample XQ-SB-2; (B) $BaSO_4$ in sample XQ-SB-2; (C) ZnS in sample MZ-SB-2; (D) PbS in sample MZ-SB-2; (E) HgS in sample CT-SB-2; (F) FeS in sample CT-SB-2.

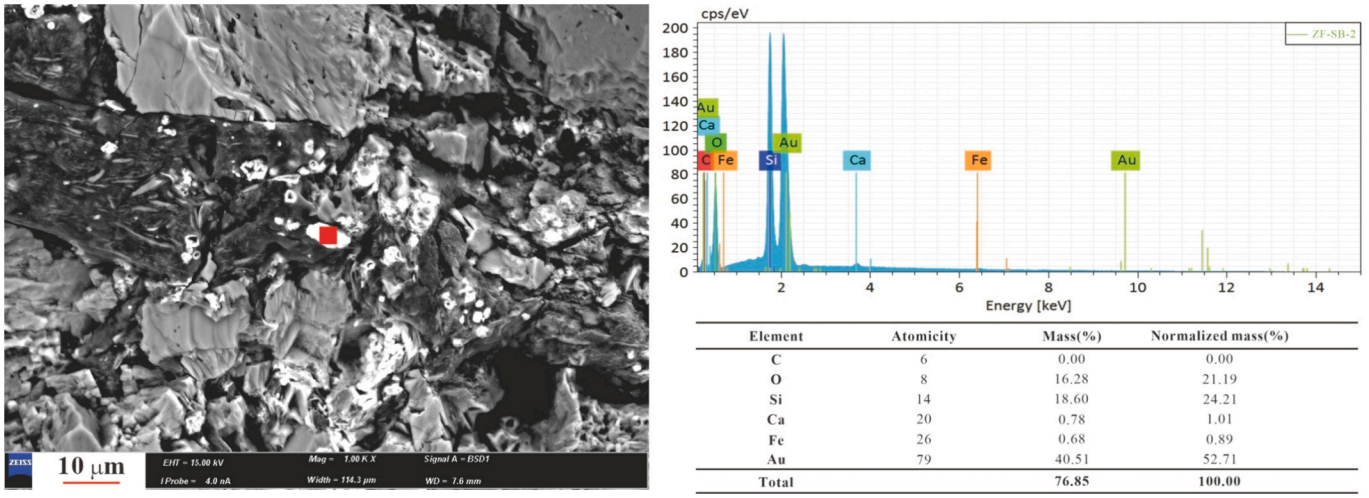

Element	Atomicity	Mass(%)	Normalized mass(%)
C	6	0.00	0.00
O	8	16.28	21.19
Si	14	18.60	24.21
Ca	20	0.78	1.01
Fe	26	0.68	0.89
Au	79	40.51	52.71
Total		76.85	100.00

Fig. 7. Energy-dispersive spectroscopy (EDS) spectra of micron-scale gold particles in sample ZF-SB-2. (For interpretation of the references to colour in this figure legend, the reader is referred to the web version of this article.)

isotope values of metal sulfides.

4.3.1. *Metallogenic age*

Extensive research on the metallogenic age of the study area has been conducted. Widely accepted methods such as Rb—Sr and Sm—Nd isotope dating were employed, providing substantial data on the metallogenic ages of numerous deposits (Fig. 9) (Li et al., 2007; Lin et al., 2010; Zhou et al., 2014). The metallogenic ages of the mineral deposits in the Xuefeng Mountains Uplift primarily date to the Caledonian epoch (490–464 Ma) and the early Hercynian epoch (410–350 Ma). Mineral deposits in the Micang-Daba Mountains Uplift experienced two mineralization phases during the Caledonian and Indosinian–Yanshanian epochs. The metallogenic ages of the mineral deposits in the Nanpanjiang Basin and Kangdian Axis date to the Indosinian–Yanshanian

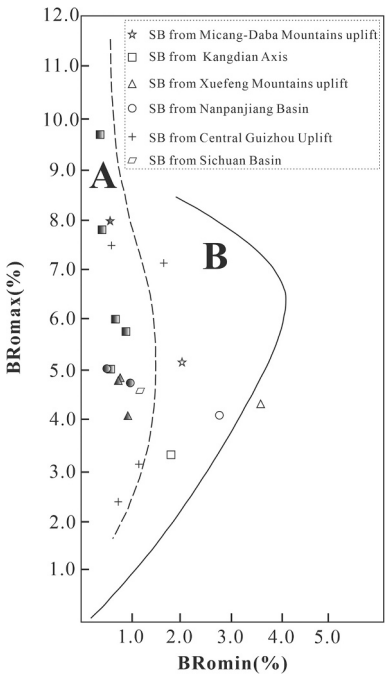

Fig. 8. Relationship between BRomax and BRomin of the solid bitumen. SB represents solid bitumen. The filling graphic symbols represent the solid bitumen is associated with ore. Region A experienced anomalous heat, while Region B was not affected. The base map was modified from Goodarzi et al. (1993).

epochs (around 200 Ma). Mineral deposits in the Lanping-Simao Basin formed in the Himalayanian epoch (27.7 Ma) (Sun et al., 2021).

4.3.2. *Metallogenic temperature: Evidence from fluid inclusions*

Recent research on the metallogenic temperatures of low- to medium-temperature hydrothermal deposits in the study area revealed that temperatures mainly ranged from 90 °C to 220 °C (Huang and Jin, 2018; Li et al., 2018; Zhang et al., 2005). We measured the homogenization temperatures of fluid inclusions in eight samples (methods followed Goldstein and Reynolds (1994)): KSL—Ca—2, YB-Ca-4, and GT-Ca-2 represented hydrothermal calcite with solid bitumen; MZ-Ca-3, TBS—Ca—2, and XQ-Ca-3 corresponded to lead–zinc deposit samples; DGL—Ca—3 and CT-Ca-2 were mercury deposit samples; and ZF-Ca-3 was a disseminated gold deposit sample (Table 4).

The results showed that temperatures ranged from 115 °C to 176 °C, consistent with previous findings (90–220 °C). Notably, paleo-oil reservoirs and these mineral deposits were closely related spatially, often sharing reservoir space or exhibiting a pattern of oil overlying minerals. However, the temperatures reconstructed from inclusions in paleo-oil reservoirs were much lower than the metallogenic temperatures. For example, the Mayuan lead–zinc deposit and the Micang Mountains paleo-oil reservoir, both located in the Sinian Dengying Formation, exhibited significantly different inclusion temperature data.

The paleo-oil reservoir temperature results ranged from 123 °C to 138 °C (Sample YB-Ca-4), while the metallogenic temperature results for the lead–zinc deposit ranged from 195 °C to 309 °C (Wang et al., 2008). Similarly, in the Nanpanjiang Basin, paleo-oil reservoir temperatures ranged from 134 °C to 158 °C (Sample GT-Ca-2), consistent with existing findings that range from 90 °C to 160 °C (Gu et al., 2007). In contrast, inclusion temperatures from disseminated gold deposits related to organic matter ranged from 150 °C to 250 °C (Gu et al., 2007). These findings indicated that metallogenic fluid temperatures were higher than those of the paleo-oil reservoir fluids, supporting the existence of strong optical anisotropy in the solid bitumen associated with minerals.

4.3.3. *Sulfur isotope of the metal sulfide mineral*

The low- to medium-temperature hydrothermal minerals investigated in this study were sphalerite (ZnS), galena (PbS), and cinnabar (HgS). In disseminated gold deposits, gold primarily existed as colloidal dispersions on pyrite particles composed of FeS_2. Therefore, understanding the sulfur source was essential for studying the sources of ore-forming materials and reconstructing the metallogenic process. For specific research topics, sulfur sources were identified using sulfur isotope tracing methods.

We measured the $\delta^{34}S_{CDT}$ values of seven samples (Table 5). The sulfur isotopic compositions showed significant variation, with the LP-sp-3 sample having a value of −7.26 ‰ and the DGL-sp-2 sample having a value of 30.17 ‰, indicating the complexity of the sulfur sources (Fig. 10).

Although variations exist in the sulfur isotopic compositions of metallic sulfides across different deposits and among distinct minerals within the same deposit (Fig. 10), most samples exhibited positive $\delta^{34}S_{CDT}$ values, potentially reflecting the source of sulfur. Stratiform mercury deposits from the Xuefeng Mountains Uplift showed $\delta^{34}S_{CDT}$ values of 24.72 ‰ (Sample CT-ci-1), while MVT deposits exhibited $\delta^{34}S_{CDT}$ values of 30.17 ‰ (Sample DGL-sp-2) and 27.22 ‰ (Sample DGL-ga-2). These values align with existing research that reports a range

Table 3
Elemental composition of solid bitumen samples.

Location	Sample ID	Associated Ore	C (%)	H (%)	O (%)	N (%)	S (%)	H/C atomic ratio	O/C atomic ratio	S/C atomic ratio
Sichuan Basin	WY-SB-2	None	83.36	2.50	1.85	0.43	3.50	0.357	0.017	0.016
Longmen Orogenic Belt	TB-SB-1	None	53.58	5.08	4.46	0.60	2.07	1.130	0.062	0.014
Micang-Daba Mountains Uplift	YB-SB-3	None	82.94	2.40	7.75	0.36	3.65	0.345	0.070	0.016
	MY-SB-2	Sphalerite	82.15	2.84	4.81	0.75	7.05	0.412	0.044	0.032
Xuefeng Mountains Uplift	WS-SB-1	Cinnabar	85.07	2.76	3.92	0.81	7.16	0.387	0.035	0.032
	DGL-SB-2	Sphalerite	84.31	2.92	2.79	0.77	6.60	0.413	0.025	0.029
	CT-SB-1	Cinnabar	82.67	3.35	2.22	0.85	6.59	0.483	0.020	0.030
	ST-SB-3	None	86.55	2.56	6.69	0.75	1.07	0.352	0.058	0.005
Central Guizhou Uplift	DZ-SB-3	None	46.53	2.84	8.42	0.69	1.51	0.727	0.136	0.012
	YK-SB-1	None	88.31	2.55	4.17	0.47	3.66	0.344	0.035	0.016
	PB-SB-2	None	82.83	2.67	4.78	0.50	4.14	0.384	0.043	0.019
Nanpanjiang Basin	MJ-SB-2	None	87.54	3.60	1.89	0.87	3.82	0.490	0.016	0.016
	GT-SB-1	None	33.67	2.29	10.20	0.24	1.85	0.810	0.227	0.021
	CH-SB-4	Disseminated Au	72.58	2.59	10.88	0.79	5.91	0.425	0.113	0.031
	ZF-SB-2	Disseminated Au	75.93	2.63	9.14	0.06	6.66	0.413	0.090	0.033
Kangdian Axis	MP-SB-1	Galena	86.53	3.35	2.65	0.34	6.88	0.461	0.023	0.030
	CP-SB-3	Sphalerite	79.17	2.26	4.21	0.48	6.74	0.340	0.040	0.032
	HD-SB-1	None	86.81	3.44	1.93	0.63	4.57	0.472	0.017	0.020
	MZ-SB-2	Galena	79.54	1.91	6.85	0.32	6.28	0.286	0.065	0.030
Lanping-Simao Basin	LP-SB-3	Sphalerite	74.30	5.92	8.35	0.69	6.16	0.949	0.084	0.031

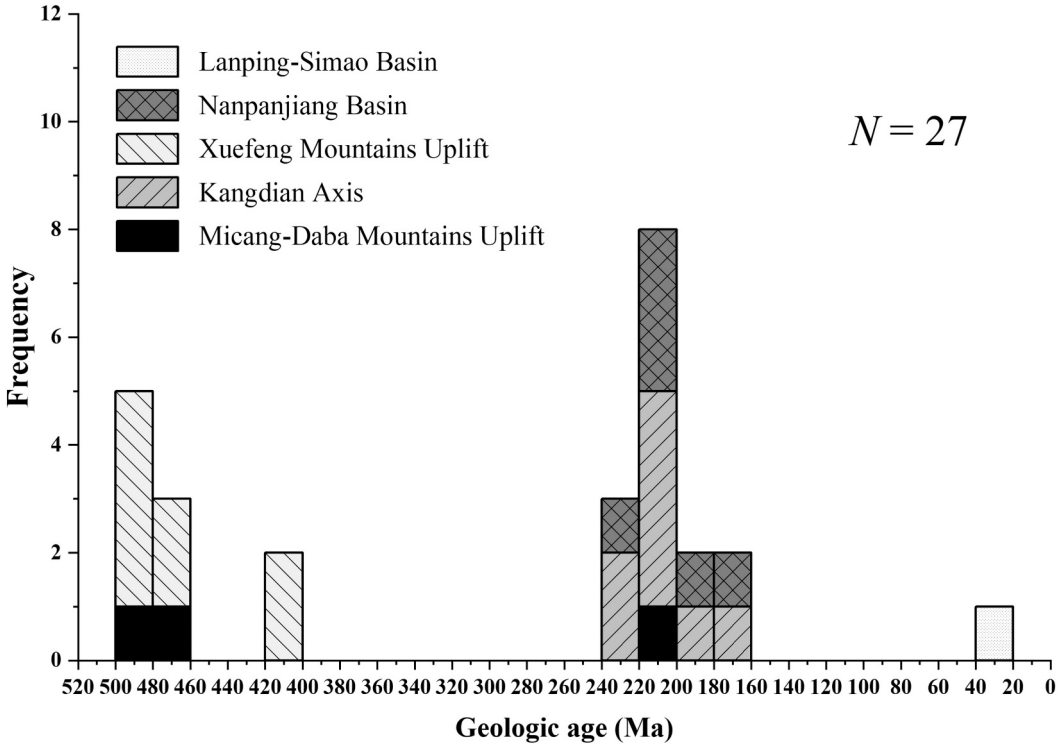

Fig. 9. Summary of chronological data on low- and medium-temperature hydrothermal ore-formation in Southwest China, as reported in the literature.

Table 4
Fluid inclusion homogenization temperatures of the Symbiotic mineral.

Sample ID	Mineral	Occurrence	Th (°C)	n
KSL-Ca-2	calcite	Bituminous vein	127–157/140.2	19
YB-Ca-4	calcite	Bituminous vein	123–138/129.7	18
DGL-Ca-3	calcite	Calcite vein with cinnabar	115–148/134.5	22
GT-Ca −2	calcite	Bituminous vein	134–158/149.1	22
ZF-Ca-3	calcite	Calcite vein with disseminated Au	146–170/162.9	24
TBS-Ca-22	calcite	Calcite vein with sphalerite	136–176/152.0	22
XQ-Ca-3	calcite	Calcite vein with sphalerite	127–148/139.6	19
MZ-Ca-3	calcite	Calcite vein with sphalerite	123–175/155.5	24

from 19.10 ‰ to 31.33 ‰ (Li, 1992; Luo et al., 2009; Ye et al., 2005). In contrast, mineral deposits from the Kangdian Axis showed $\delta^{34}S_{CDT}$ values of 9.66 ‰ (Sample MZ-ga-2) and 14.01 ‰ (Sample MZ-sp-2), consistent with previous reports ranging between 4.24 ‰ and 17.68 ‰ (He et al., 2016; Li et al., 2004a; Zhou et al., 2012).

In contrast, Li et al. (2007) reported $\delta^{34}S_{CDT}$ values between 17.7 ‰ and 19.4 ‰ and an Rb—Sr dating result of 486 Ma for MVT deposits from the Micang–Daba Mountains Uplift, while Wang et al. (2008) reported $\delta^{34}S_{CDT}$ values between 15.6 ‰ and 18.0 ‰. Among the two Micang-Daba Mountains Uplift samples analyzed in this study, the galena sample exhibited a $\delta^{34}S_{CDT}$ value of 13.34 ‰ (Sample MY-sp-2), which aligns closely with previous research findings. In contrast, the sphalerite sample showed a $\delta^{34}S_{CDT}$ value of −2.74 ‰, which differed significantly from the existing findings. These results suggest that the MVT deposits in the Micang-Daba Mountains Uplift originated from at least two distinct sulfur sources (Fig. 10), indicative of varying metallogenic times and temperatures.

The $\delta^{34}S_{CDT}$ values of mineral deposits from the Lanping–Simao Basin ranged from −29.00 ‰ to −1.33 ‰ (Chen, 2015), consistent with the results of this study (Sample LP-sp-3). Overall, the values were relatively negative, indicating that the mineral deposits in the Lanping–Simao Basin originated from a different sulfur source than the MVT deposits in the Xuefeng Mountains Uplift and the Kangdian Axis. The $\delta^{34}S_{CDT}$ values of mineral deposits from the Nanpanjiang Basin exhibited the widest range, from −21.2 ‰ to 21 ‰ (Wang et al., 2010; Yuan et al., 1997), indicating a complex metallogenic process.

4.4. Timing of metallogenesis and hydrocarbon accumulation

The relationships between metal mineralization and reservoir formation can be categorized into three scenarios: (1) hydrocarbon accumulation preceded metal mineralization; (2) metal mineralization and hydrocarbon accumulation occurred nearly simultaneously; and (3) hydrocarbon accumulation followed metal mineralization. The third scenario, in which hydrocarbon accumulation is unrelated to metal mineralization or merely follows mineralizing fluids, is rare in nature and likely coincidental (Parnell, 1991, 1994). The first two scenarios suggest a close genetic relationship between metal mineralization and hydrocarbon accumulation and are, therefore, the focus of this discussion.

4.4.1. Timing of hydrocarbon accumulation/destruction

In southwest China, primary oil was generated at 400–480 Ma from the Lower Cambrian shale ($\in_1$n), and oil cracking in ancient reservoirs began around 200 Ma (Wei et al., 2020), except for the paleo-oil reservoir in the Sichuan Basin, which started at 85 Ma (Li et al., 2015). Sun et al. (2024) reported that the solid bitumen from the Sichuan Basin has a *Re*—Os age of 342.8 Ma, indicating the timing of hydrocarbon accumulation. In contrast, the solid bitumen from the Xuefeng Mountains Uplift has a Re—Os age of 195 Ma, representing the timing of oil cracking. Wu et al. (2013) reported that solid bitumen not associated with sulfide minerals has a Re—Os age of 292.0 Ma, indicating the timing of hydrocarbon accumulation, whereas solid bitumen

Table 5
Sulfur isotope values of sulfide minerals.

Sample ID	Location	Mineral	$\delta^{34}S_{CDT}$ (‰)	Metallogenic age (Ma)
MY-sp-2	Micang-Daba Mountains Uplift	Sphalerite	−2.74	206 (Wang et al., 2015)
MY-ga-2		Galena	13.34	
MAYN		Sphalerite	17.7–19.4 (Li et al., 2007)	486 (Li et al., 2007)
S-1		Sphalerite	16.0–18.0 (Wang et al., 2008)	468 (Wang et al., 2015)
F-1		Galena	15.6–16.8 (Wang et al., 2008)	
DGL-sp-2		Sphalerite	30.17	489 (Zhou et al., 2014)
DGL-ga-2		Galena	27.22	
CT-ci-1	Xuefeng Mountains Uplift	Cinnabar	24.72	487 (Zhou et al., 2014)
LM		Sphalerite	20.30–31.33 (Luo et al., 2009)	477 (Yu et al., 2017)
XN		Galena	19.10–28.50 (Li, 1992)	490 (Du et al., 2012)
L-2		Sphalerite	24.12–29.81 (Ye et al., 2005)	
ZF-py-2	Nanpanjiang Basin	Pyrite	5.11	204 (Chen et al., 2015)
GT-2		Pyrite	−21.2–-13.29 (Yuan et al., 1997)	172 (Liu and Geng, 1985)
SYD		Pyrite	1.6–21 (Wang et al., 2010)	235 (Chen et al., 2015)
MZ-sp-2	Kangdian Axis	Sphalerite	14.01	
MZ-ga-2		Galena	9.66	
MZ-5		Galena	14.21–15.37 (Zhou et al., 2012)	194 (Zhou et al., 2012)
TBS-14		Sphalerite	4.24–4.87 (He et al., 2016)	
HZ-911		Sphalerite	12.53–17.68 (Li et al., 2004a)	226 (Li et al., 2004b)
LP-sp-3	Lanping-Simao Basin	Sphalerite	−7.26	28 (Sun et al., 2021)
LP-1		Galena	−29.00–-1.33 (Chen, 2015)	

associated with sulfide minerals has a Re—Os age of 165–200 Ma, representing the timing of bitumen solidification. This timing is close to the Rb—Sr age of sulfide minerals at 201 Ma (Zhang et al., 2014).

4.4.2. Implications from sulfur isotopes

In low- to mid-temperature hydrothermal mineral deposits without magmatic involvement, the source of sulfur and the timing of mineralization remain unclear. Common reactions that supply reduced sulfur for mineral precipitation from marine sulfate include bacterial sulfate reduction (BSR) and thermochemical sulfate reduction (TSR), both of which require organic matter (Cai et al., 2003; Krouse et al., 1988). BSR occurred at temperatures not exceeding 80 °C when hydrocarbons were immature to low maturity (Machel, 2001), whereas TSR required a minimum temperature of 127 °C and was associated with higher hydrocarbon maturity (Machel, 2001).

Sulfur in a deposit can be derived from one or more sources. Variability in sulfur sources, reduction processes, or differing physicochemical conditions within a single process can cause significant sulfur isotopic fractionation between sulfate and reduced sulfur. BSR-induced sulfur isotopic fractionation ranged from +4 ‰ to +46 ‰ with an average value of 21 ‰ (Canfield and Thamdrup, 1994). The lower the temperature, the more pronounced the degree of isotopic fractionation. TSR-induced fractionation ranged from +10 ‰ to +20 ‰ (Machel et al., 1995). In some instances, reduced sulfur may have originated from the thermal decomposition of sulfur-containing organic matter (TDS), which typically exhibits negative isotopic values. For example, in certain gas fields within the Sichuan Basin, the $\delta^{34}S_{CDT}$ values of sulfides in solid bitumen ranged from −4.6 ‰ to +0.9 ‰ (Cai et al., 2010).

The host strata of the deposits in the Micang Mountains Uplift and Kangdian Axis primarily consisted of Sinian Dengying Formation (Z_2dn) dolomites, with marine sulfate $\delta^{34}S_{CDT}$ compositions ranging from +20.2 ‰ to +38.7 ‰ and an average of approximately +29 ‰ (Zhang et al., 2004). The host strata of the Xuefeng Mountains Uplift deposits mainly consisted of middle to upper Cambrian dolomites, with marine sulfate $\delta^{34}S_{CDT}$ values ranging from +27 ‰ to +32 ‰ (Claypool et al., 1980). The marine sulfate $\delta^{34}S_{CDT}$ compositions of the two regions were quite similar.

The $\delta^{34}S_{CDT}$ values of the lead–zinc ores in the Xuefeng Mountains Uplift ranged from +19.10 ‰ to +31.33 ‰ (Fig. 10), resembling the isotopic fractionation results of TSR. The maturity of Lower Cambrian source rocks ($\in_1 n$) was low at the time of mineralizatio. The ore-forming fluid accelerated the thermal evolution of the Lower Cambrian source rocks and facilitated hydrocarbon formation, which effectively concentrated lead and zinc from the source rock (Sicree and Barnes, 1996). As this fluid migrated into reservoirs, hydrocarbons reduced SO_4^{2-} from marine sulfate to S^{2-} via TSR, producing reduced sulfur that combined with lead and zinc to precipitate as ores (Fig. 11).

In the Kangdian Axis and Micang Mountains Uplifts, the $\delta^{34}S_{CDT}$ values of the lead–zinc ores were lower. In addition to TSR, TDS contributed sulfur. The Lower Cambrian source rocks ($\in_1 n$) began gas generation at the time of mineralization. When the ore-forming fluid migrated into paleo-oil reservoirs containing methane and H_2S produced by high-temperature cracking (TDS), they mixed, initiating mineralization (Fig. 12). First, metal ions rapidly combined with H_2S and

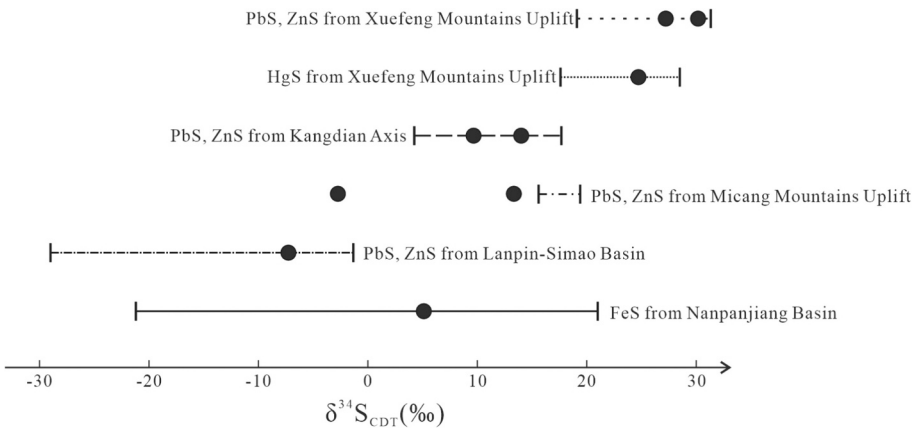

Fig. 10. $\delta^{34}S_{CDT}$ values of the sulfide deposits in southwestern China. Scale bar shows the scatter of $\Delta\delta^{34}S_{CDT}$ in the literature. Circle shows the $\delta^{34}S_{CDT}$ in this study.

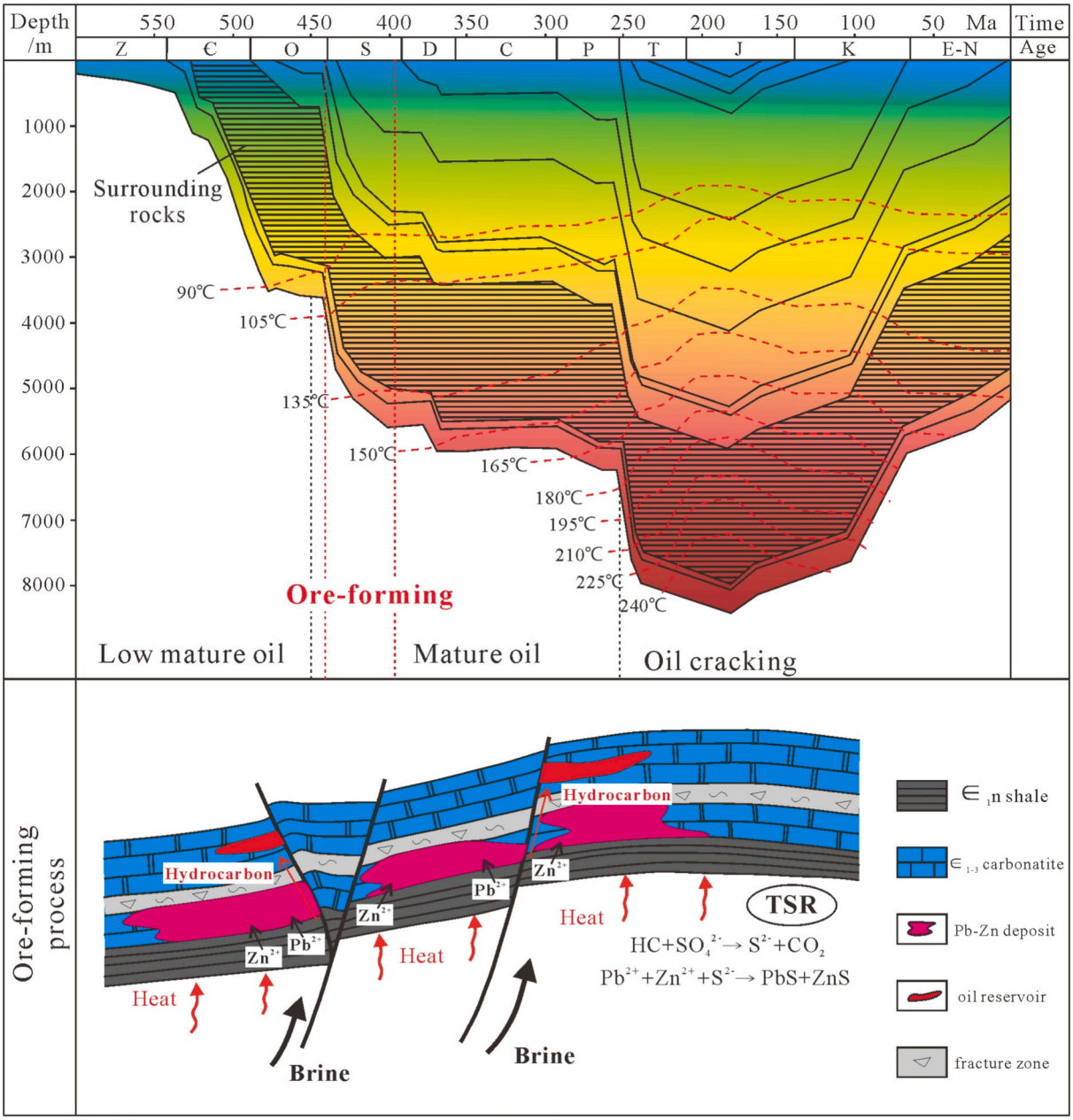

Fig. 11. Timing of the hydrocarbon formation and ore formation in the Xuefeng Mountains Uplift (burial history after Li et al. (2011), modified).

precipitated to form minerals. Consequently, the reduced sulfur during the early mineralization stage was mainly derived from TDS, leading to low $\delta^{34}S_{CDT}$ values in the metal sulfide. Second, the TSR reaction began, with hydrocarbons in the paleo-oil reservoirs acting as reducing agents and reacting with marine sulfates. The reduced sulfur combined with metal elements, producing lead–zinc minerals with high $\delta^{34}S_{CDT}$ values.

The $\delta^{34}S_{CDT}$ values of the lead–zinc ores in the Lanping-Simao Basin reached values as low as −29 ‰ (Zhao, 1989), which could only be produced by BSR. Similarly, the Navan superlarge lead–zinc deposit in Ireland had an average sulfur $\delta^{34}S_{CDT}$ value of −13.6 ‰, with over 90 % of the reduced sulfur attributed to BSR (Fallick et al., 2001). These findings indicated that BSR was important in the precipitation of lead–zinc ores in the Lanping region and that the organic matter was immature to low maturity during metallogenesis (Fig. 13). Chen (2015) conducted sulfur isotope analysis on lead–zinc ores in the Lanping Basin, revealing that the deposit formed through two metallogenic stages. The first-stage sulfides exhibited low $\delta^{34}S_{CDT}$ values (−28 ‰ to −12 ‰), marking the primary metallogenic period. The second-stage sulfides had relatively high $\delta^{34}S_{CDT}$ values (−6 ‰ to 0 ‰), indicating that the sulfur source may have changed as organic matter maturity increased (Chen, 2015).

The $\delta^{34}S_{CDT}$ values of pyrite in the Nanpanjiang Basin varied significantly, likely due to the complex metallogenic processes associated with Carlin-type gold deposits. The methods of sulfur supply differed across various metallogenic processes, and the maturity of organic matter varied during mineralization, contributing to the complexity of metallogenesis in the region.

The $\delta^{34}S_{CDT}$ values of sulfide minerals can represent the source of sulfur, which is determined by the maturity of hydrocarbons. When $\delta^{34}S_{CDT} < 0$ ‰, the sulfur was primarily derived from BSR, and the associated organic matter was in an immature to early mature stage. When $\delta^{34}S_{CDT} < 10$ ‰, the sulfur was predominantly derived from TDS, and the associated organic matter was in a highly mature to overmature stage. When $\delta^{34}S_{CDT} > 20$ ‰, the sulfur was mainly derived from TSR,

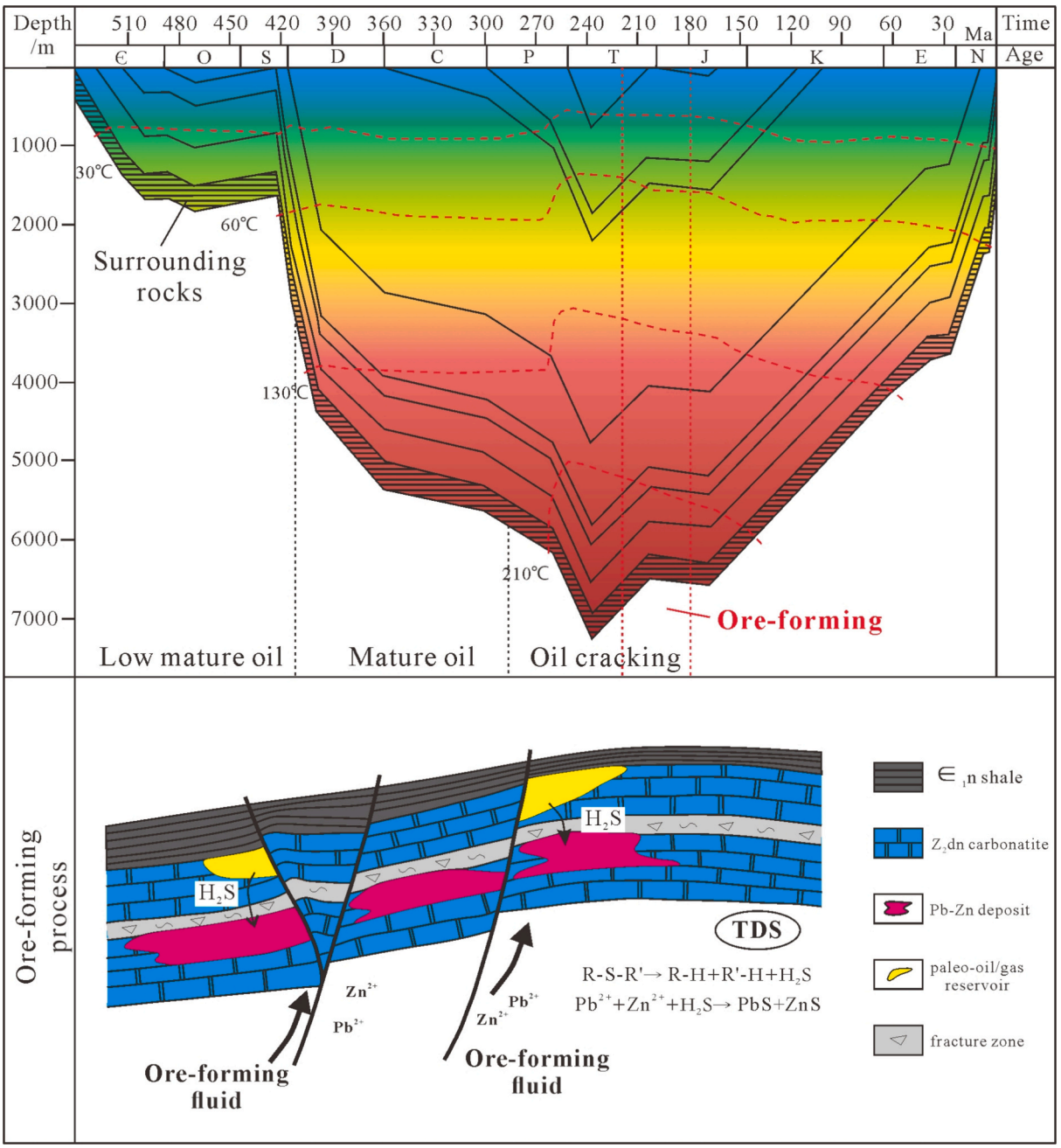

Fig. 12. Timing of the hydrocarbon formation and ore formation in the Kangdian Axis (burial history after Wang (2015), modified).

and the associated organic matter was in a mature stage. During different stages of mineralization within the same deposit, the sources of sulfur may have varied.

During mineralization, if organic matter had not yet entered the oil window, the source rock could still generate and expel oil in response to the heat provided by mineralizing fluids. This generated oil subsequently migrated with the mineralizing fluids into suitable reservoirs, facilitating both mineralization and hydrocarbon accumulation, with sulfur primarily derived from BSR (Fig. 13). If organic matter was in a mature stage, mineralization generated elevated heat that facilitated oil formation, while hydrocarbon accumulation enhanced the extraction and concentration of mineralizing elements, creating a complementary relationship between the two processes. Organic matter reduced SO_4^{2-} to S^{2-} from marine sulfate via TSR, resulting in the reforming of the paleo-oil reservoir (Fig. 11).

If organic matter was in a highly mature to overmature stage, when ore-forming fluids migrated into paleo-oil/gas reservoirs containing methane and H_2S produced by high-temperature cracking (TDS), they mixed, initiating mineralization and severely impacting ancient oil reservoirs (Fig. 12). The mode of reduced sulfur supply shifted to TSR over time due to the consumption of H_2S derived from TDS in ancient oil/gas reservoirs. In conclusion, the ore-forming process enhanced the thermal maturity of organic matter, leading to hydrocarbon accumulation and destruction. Organic matter provided and reduced sulfur for metallogenesis through different processes, which is reflected in sulfur isotopes.

5. Conclusions

Solid bitumen and low- to medium-temperature hydrothermal metallic minerals were widely associated with hydrocarbon reservoir rocks in Southwest China. The association patterns of solid bitumen and

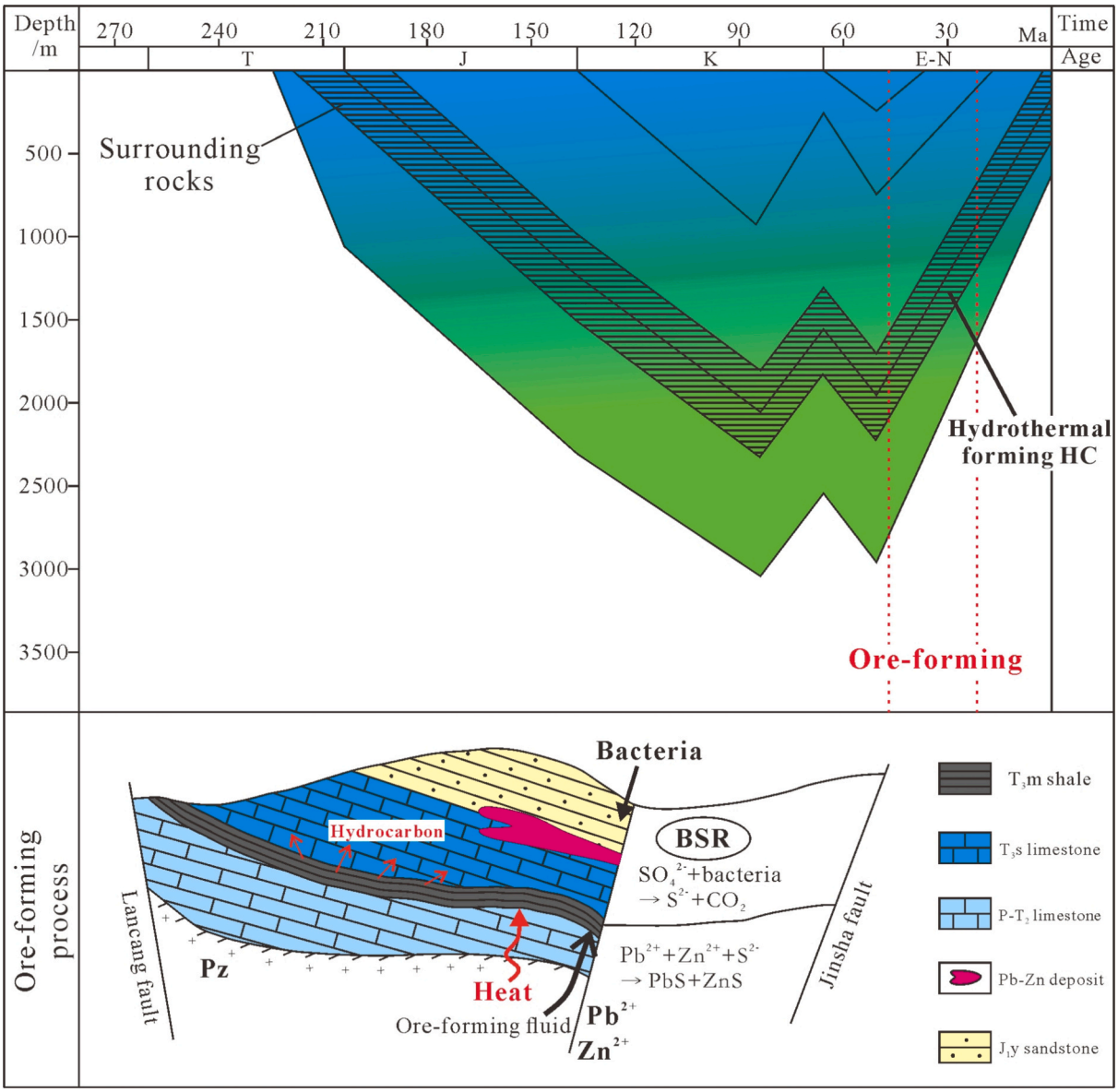

Fig. 13. Timing of the hydrocarbon formation and ore formation in the Lanping-Simao Basin (burial history after Zhao (1989), modified).

metallic minerals were categorized into MVT deposits associated with solid bitumen, stratiform mercury deposits associated with solid bitumen, and disseminated gold deposits associated with solid bitumen. Solid bitumen, as a byproduct of hydrocarbons reformed by metallogenic processes, exhibited strong optical anisotropy and a high S/C ratio.

The sulfur isotopes of sulfide ores indicated distinct sulfur sources and the thermal maturity of organic matter during metallogenesis. The $\delta^{34}S_{CDT}$ values of sulfide ores from MVT deposits associated with solid bitumen in the Lanping-Simao Basin were less than 0 ‰, indicating that sulfur was primarily derived from BSR, and the associated organic matter was in an immature to early mature stage. The ore-forming fluid enhanced the thermal maturity of hydrocarbons and promoted the formation of oil. The $\delta^{34}S_{CDT}$ values of sulfide ores from MVT deposits associated with solid bitumen in the Kangdian Axis were less than 20 ‰, indicating that sulfur was predominantly derived from TDS and TSR, with the associated organic matter in a highly mature to overmature stage.

The heat from ore-forming fluids caused oil cracking and severe destruction of paleo-oil reservoirs. The $\delta^{34}S_{CDT}$ values of sulfide ores from MVT deposits associated with solid bitumen and stratiform mercury deposits associated with solid bitumen in the Xuefeng Mountains Uplift were mostly greater than 20 ‰, indicating that sulfur was primarily derived from TSR and that the associated organic matter was in a mature stage. Mineralization generated elevated heat that facilitated oil formation, while hydrocarbon accumulation enhanced the extraction and concentration of mineralizing elements. During different stages of metallogenesis within the same deposit, the sources of sulfur may have varied. Metallic mineralization accelerated the thermal maturity of organic matter, reformed paleo-oil reservoirs, and facilitated oil cracking. Furthermore, organic-inorganic interactions played a key role in the formation and precipitation of metal sulfides.

CRediT authorship contribution statement

Wen Sun: Writing – review & editing, Writing – original draft, Visualization, Methodology, Investigation, Data curation, Conceptualization. **Ningning Zhong:** Supervision, Resources, Project administration, Funding acquisition, Conceptualization. **Yongli Lu:** Investigation. **Dahua Li:** Resources. **Qingyong Luo:** Conceptualization. **Lipeng Yao:**

Investigation. **Yanan Yang:** Data curation. **Chunfang Cai:** Data curation. **Zilong Fang:** Investigation.

Declaration of competing interest

The authors declare that they have no known financial conflicts of interest or personal relationships that could influence the findings reported in this paper.

Acknowledgments

This study was supported by the National Key Research and Development Program of China (No. 2017YFC0603102) and the National Natural Science Foundation of China (No. 42122016, No. 42302172). The authors gratefully acknowledge Jianfa Chen for assisting with sample collection.

Data availability

Data will be made available on request.

References

Cai, C., Worden, R.H., Bottrell, S.H., Wang, L., Yang, C., 2003. Thermochemical sulphate reduction and the generation of hydrogen sulphide and thiols (mercaptans) in Triassic carbonate reservoirs from the Sichuan Basin, China. Chem. Geol. 202, 39–57. https://doi.org/10.1016/S0009-2541(03)00209-2.

Cai, C., Li, K., Zhu, Y., Xiang, L., Jiang, L., Tenger Cai, X., Cai, L., 2010. TSR origin of sulfur in Permian and Triassic reservoir bitumen, East Sichuan Basin, China. Org. Geochem. 41, 871–878. https://doi.org/10.1016/j.orggeochem.2010.03.009.

Canfield, D.E., Thamdrup, B., 1994. The production of 34S-depleted sulfide during bacterial disproportionation of elemental sulfur. Science 266, 1973–1975. https://doi.org/10.1126/science.11540246.

Carrie, J., Sanei, H., Stern, G., 2012. Standardisation of Rock-Eval pyrolysis for the analysis of recent sediments and soils. Org. Geochem. 46, 38–53. https://doi.org/10.1016/j.orggeochem.2012.01.011.

Chen, Y., 2015. Sulfur Isotope Geochemical Characteristics of Jinding Lead–Zinc Deposit in Yunnan and its Metallogenic Significance. Masters Thesis. China University of Geosciences Beijing.

Chen, M., Mao, J., Li, C., Zhang, Z., Dang, Y., 2015. Re-Os isochron ages for arsenopyrite from Carlin-like gold deposits in the Yunnan-Guizhou-Guangxi "golden triangle", southwestern China. Ore Geol. Rev. 64, 316–327. https://doi.org/10.1016/j.oregeorev.2014.07.019.

Claypool, G.E., Holser, W.T., Kaplan, I.R., Sakai, H., Zak, I., 1980. The age curves of sulfur and oxygen isotopes in marine sulfate and their mutual interpretation. Chem. Geol. 28, 199–260. https://doi.org/10.1016/0009-2541(80)90047-9.

Craddock, P.R., Rouxel, O.J., Ball, L.A., Bach, W., 2008. Sulfur isotope measurement of sulfate and sulfide by high-resolution MC-ICP-MS. Chem. Geol. 253, 102–113. https://doi.org/10.1016/j.chemgeo.2008.04.017.

Ding, T., Valkiers, S., Kipphardt, H., De Bievre, P., Taylor, P., Gonfiantini, R., Krouse, R., 2001. Calibrated sulfur isotope abundance ratios of three IAEA sulfur isotope reference materials and V-CDT with a reassessment of the atomic weight of sulfur. Geochim. Cosmochim. Acta 65, 2433–2437. https://doi.org/10.1016/S0016-7037(01)00611-1.

Du, G.M., Cai, H., Mei, Y.P., 2012. Application of RB-SR isochron dating method in sphalerite of sulphide deposit-a case study from Dagoudong PB-ZN deposit in xinhuang,western Hunan Province. South China Geol. 28, 175–180. https://doi.org/10.3969/j.issn.1007-3701.2012.02.011.

Espitalié, J., Laporte, J., Madec, M., Marquis, F., Leplat, P., Paulet, J., Boutefeu, A., 1977. Méthode rapide de caractérisation des roches mètres, de leur potentiel pétrolier et de leur degré d'évolution. Rev. Inst. Fr. Pét. 32, 23–42. https://doi.org/10.2516/ogst:1977002.

Fallick, A.E., Ashton, J.H., Boyce, A.J., Ellam, R.M., Russell, M.J., 2001. Bacteria were responsible for the magnitude of the world-class hydrothermal base metal sulfide orebody at Navan, Ireland. Econ. Geol. 96, 885–890. https://doi.org/10.2113/gsecongeo.96.4.885.

Gentzis, T., Goodarzi, F., 1990. A review of the use of bitumen reflectance in hydrocarbon exploration with examples from Melville Island, Arctic Canada. In: Nuccio, V.F., Barker, C.E., Dyson, S.J. (Eds.), Rocky Mountain Section (SEPM). SEPM Society for Sedimentary Geology, Tulsa, pp. 23–36.

Goldstein, R.H., Reynolds, T.J., 1994. Fluid inclusion microthermometry. In: Robert, H. G., Reynolds, T.J. (Eds.), Systematics of Fluid Inclusions in Diagenetic Minerals. SEPM Society for Sedimentary Geology, Tulsa, pp. 87–121.

Goodarzi, F., Gentzis, T., Jackson, G., Macqueen, R.W., 1993. Optical characteristics of heat-affected bitumens from the Nanisivik Mine, NW Baffin Island, Arctic Canada. Energy Sources 15, 359–376. https://doi.org/10.1080/00908319308909031.

Greenwood, P.F., Shan, C., Holman, A.I., Grice, K., 2018. The composition and radiolysis impact on aromatic hydrocarbons in sedimentary organic matter from the Mulga Rock (Australia) uranium deposit. Org. Geochem. 123, 103–112. https://doi.org/10.1016/j.orggeochem.2018.06.013.

Grint, A., Marsh, H., 1981. Carbonization of coal blends: mesophase formation and coke properties. Fuel 60, 1115–1120. https://doi.org/10.1016/0016-2361(81)90063-6.

Gu, X.X., Li, B.H., Xu, S.H., Fu, S.H., Dong, S.Y., 2007. Characteristics of hydrocarbon-bearing ore-forming fluids in the Youjiang Basin, South China: implications for hydrocarbon accumulation and ore mineralization. Earth Sci. Front. 14, 133–146. https://doi.org/10.3321/j.issn:1005-2321.2007.05.014.

Gu, X.X., Zhang, Y.M., Li, B.H., Xue, C.J., Dong, S.Y., Fu, S.H., Cheng, W.B., Liu, L., Wu, C.Y., 2010. The coupling relationship between metallization and hydrocarbon accumulation in sedimentary basins. Earth Sci. Front. 17, 83–105.

He, D.F., Li, D.S., Zhang, G.W., Zhao, L.Z., Fan, C., Lu, R.Q., Wen, Z., 2011. Formation and evolution of multi-cycle superposed Sichuan Basin, China. Chin. J. Geol. 46, 589–606. https://doi.org/10.3969/j.issn.0563-5020.2011.03.001.

He, C.Z., Xiao, Z.Y., Wen, H.J., Zhou, T., Zhu, C.W., Fan, H.F., 2016. Zb-S isotopic compositions of the Tianbaoshan carbonate-hosted Pb-Zn deposit in Sichuan, China: Implications for source of ore components. Acta Petrol. Sin. 32, 3394–3406.

Huang, Y., Jin, J.C., 2018. The genesis and metallogenic model of lead-zinc deposits in northeastern Yunnan. China Met. Bull. 7, 32+34. https://doi.org/10.3969/j.issn.1672-1667.2018.07.019.

Huang, Z.L., Hu, R.Z., Su, W.C., Wen, H.J., Liu, S., Fu, Y.Z., 2011. A study on the large-scale low-temperature metallogenic domain in southwestern China-significance, history and new progress. Acta Mineral. Sin. 31, 309–314. https://doi.org/10.16461/j.cnki.1000-4734.2011.03.001.

ISO 7404-5, 2009. Methods for the Petrographic Analysis of Coals – Part 5: Method of Determining Microscopically the Reflectance of Vitrinite. International Organization for Standardization. ISO 7404-5, 2009(en). www.iso.org/standard/42832.html.

Jacob, H., 1989. Classification, structure, genesis and practical importance of natural solid oil bitumen ("migrabitumen"). Int. J. Coal Geol. 11, 65–79. https://doi.org/10.1016/0166-5162(89)90113-4.

Jochum, J., 2000. Variscan and post-Variscan lead-zinc mineralization, Rhenish Massif, Germany: evidence for sulfide precipitation via thermochemical sulfate reduction. Mineral. Deposita 35, 451–464. https://doi.org/10.1007/s001260050255.

Kesler, S., Jones, H., Furman, F., Sassen, R., Anderson, W., Kyle, J., 1994. Role of crude oil in the genesis of Mississippi Valley-type deposits: evidence from the Cincinnati arch. Geology 22, 609–612. https://doi.org/10.1130/0091-7613(1994)022<0609:ROCOIT>2.3.CO;2.

Krouse, H.R., Viau, C.A., Eliuk, L.S., Ueda, A., Halas, S., 1988. Chemical and isotopic evidence of thermochemical sulphate reduction by light hydrocarbon gases in deep carbonate reservoirs. Nature 333, 415–419. https://doi.org/10.1038/333415a0.

Leach, D.L., Bradley, D., Lewchuk, M.T., Symons, D.T., De Marsily, G., Brannon, J., 2001. Mississippi Valley-type lead-zinc deposits through geological time: implications from recent age-dating research. Mineral. Deposita 36, 711–740. https://doi.org/10.1007/s001260100208.

Li, Z.F., 1992. Isotopic composition of Pb and sulfur in the Hunan-Guizhou border lead-zinc ore belt. Guizhou Geol. 9, 246–254.

Li, W.B., Huang, Z.L., Chen, J., Xu, C., Guan, T., Yin, M.D., 2004a. Sulfur isotopes and rare-earth elements geochemistry of the giant Huize Zn-Pb deposit in Yunnan Province. Acta Geol. Sin. 78, 507–518. https://doi.org/10.3321/j.issn:0001-5717.2004.04.010.

Li, W.B., Huang, Z.L., Wang, Y.X., Chen, J., Han, R.S., Xu, C., Guan, T., Yin, M.D., 2004b. Age of the giant Huize Zn-Pb deposits determined by Sm-Nd dating of hydrothermal calcite. Geol. Rev. 50, 189–195. https://doi.org/10.3321/j.issn:0371-5736.2004.02.011.

Li, H.M., Chen, Y.C., Wang, D.H., Li, H.Q., 2007. Geochemistry and mineralization age of the Mayuan zinc deposit, Nanzheng, southern Shaanxi, China. Geol. Bull. China 26, 546–552. https://doi.org/10.3969/j.issn.1671-2552.2007.05.006.

Li, Z.Q., Liu, J., Li, Y., Hang, W.Y., Hong, H.T., Ying, D.L., Chen, X., Liu, R., Duan, X.G., 2015. Formation and evolution of Weiyuan-Anyue extension-erosion groove in Sinian system, Sichuan Basin. Pet. Explor. Dev. 42, 26–33. https://doi.org/10.11698/PED.2015.01.03.

Li, K., Zhao, S., Tang, Z., Duan, Q., Li, J., 2018. Fluid sources and ore genesis of the Pb-Zn deposits of Huayuan ore-concentrated District, Northwest Hunan Province, China. Earth Sci. 43, 2449–2464.

Li, Y., Zhong, N., Lin, J., Long, Y., Li, J., 2011. Accumulation of Upper Cambrian ancient reservoir in Wangcun, southern margin of middle Yangtze region. Petrol Geol Exp 33 (4), 408–413. https://doi.org/10.11781/sysydz201104408.

Lin, Z.Y., Wang, D.H., Zhang, C.Q., 2010. Rb-Sr isotopic age of sphalerite from the Paoma lead-zinc deposit in Sichuan Province and its implications. Geol. China 37, 488–494. https://doi.org/10.3969/j.issn.1000-3657.2010.02.023.

Liu, D.S., Geng, W.H., 1985. On the mineral association and mineralization conditions of the carlin type gold deposits in China. Geochimica 1, 277–282. https://doi.org/10.19700/j.0379-1726.1985.03.012. +295–296.

Luo, W., Yin, Z., Kong, L., Dai, T.G., 2009. Discussion on the geological features and genesis of the Limei Pb-Zn ore concentration belt in Northwestern Hunan Province. North China Geol. 32, 194–202. https://doi.org/10.3969/j.issn.1672-4135.2009.03.005.

Luo, Q., Zhang, L., Zhong, N., Wu, J., Goodarzi, F., Sanei, H., Skovsted, C.B., Suchý, V., Li, M., Ye, X., 2021. Thermal evolution behavior of the organic matter and a ray of light on the origin of vitrinite-like maceral in the Mesoproterozoic and lower Cambrian black shales: Insights from artificial maturation. Int. J. Coal Geol. 244, 103813. https://doi.org/10.1016/j.coal.2021.103813.

Machel, H.G., 2001. Bacterial and thermochemical sulfate reduction in diagenetic settings—old and new insights. Sediment. Geol. 140, 143–175. https://doi.org/10.1016/S0037-0738(00)00176-7.

Machel, H.G., Krouse, H.R., Sassen, R., 1995. Products and distinguishing criteria of bacterial and thermochemical sulfate reduction. Appl. Geochem. 10, 373–389. https://doi.org/10.1016/0883-2927(95)00008-8.

Parnell, J., 1991. Timing of hydrocarbon-metal interactions during basin evolution. In: Proceedings of the 25 Years SGA Anniversary Meeting, vol. 25, pp. 573–576.

Parnell, J., 1994. Hydrocarbons and other fluids: paragenesis, interactions and exploration potential inferred from petrographic studies. Geol. Soc. Spec. Publ. 78, 275–291. https://doi.org/10.1144/GSL.SP.1994.078.01.19.

Peters, K.E., 1986. Guidelines for evaluating petroleum source rock using programmed pyrolysis. AAPG Bull. 70, 318–329. https://doi.org/10.1306/94885688-1704-11D7-8645000102C1865D.

Rogers, M., McAlary, J., Bailey, N., 1974. Significance of reservoir bitumens to thermal-maturation studies, Western Canada Basin. AAPG Bull. 58, 1806–1824. https://doi.org/10.1306/83D919B6-16C7-11D7-8645000102C1865D.

Sanei, H., 2020. Genesis of solid bitumen. Sci. Rep. 10, 15595. https://doi.org/10.1038/s41598-020-72692-2.

Sicree, A., Barnes, H., 1996. Upper Mississippi Valley district ore fluid model: the role of organic complexes. Ore Geol. Rev. 11, 105–131. https://doi.org/10.1016/0169-1368(95)00018-6.

Sun, P.C., Li, C., Zhou, L.M., Qu, W.J., Wang, D.H., Gao, L., Li, W., Li, X.W., Zhao, H., Du, A.D., 2021. Dating metallogenic age of Jinding Pb-Zn deposit in Yunnan: evidence from Re-Os isotope of bitumen. Earth Sci. 46, 4247–4259.

Sun, W., Zhong, N., Luo, Q., Ran, Y., Zhang, Y., Wu, J., Zou, Y., Du, T., Shi, R., Hu, W., 2024. Re-Os isotopic composition characteristics and geochemical significance of reservoir solid bitumen in the Upper Yangtze region. Nat. Gas Geosci. 1, 1–25.

Sverjensky, D.A., 1986. Genesis of Mississippi Valley-type lead-zinc deposits. Annu. Rev. Earth Planet. Sci. 14, 177–199. https://doi.org/10.1146/annurev.ea.14.050186.001141.

Wang, X.H., Xue, C.J., Li, Z.M., Li, Q., Yang, R.J., 2008. Geological and geochemical characteristics of Mayuan Pb-Zn ore deposit on northern margin of Yangtze landmass. Mineral Deposits 27, 37–48. https://doi.org/10.3969/j.issn.0258-7106.2008.01.004.

Wang, Y., 2015. The Research of Shale Gas Accumulation Characteristics of The Qiongzhusi Formation, Qujing Area, Eastern Yunnan Province. Masters Thesis. China University of Mining and Technology.

Wang, C.H., Wang, D.H., Liu, J.Z., Deng, Y.M., Liu, C.Q., Li, J.K., Chen, F.E., Zhang, J.Z., 2010. Characteristics of isotopic geochemistry of Shuiyindong super-large Carlin gold deposit in Guizhou. Earth Sci. Front. 17, 396–403.

Wang, G.Z., Zhao, F.F., Fu, Y.Z., Li, N., Long, T., Xu, P., 2015. Determination of metallogenic epoch of MVT lead–zinc deposit in Dengying Formation, northern margin of Sichuan Basin. Acta Mineral. Sin. 35, 723. https://doi.org/10.16461/j.cnki.1000-4734.2015.s1.533.

Wei, G., Yang, W., Liu, M., Xie, W., Jin, H., Wu, S., Su, N., Shen, J., Hao, C., 2020. Distribution rules, main controlling factors and exploration directions of giant gas fields in the Sichuan Basin. Nat. Gas Ind. B 7, 1–12. https://doi.org/10.1016/j.ngib.2020.01.001.

Wu, Y., Zhang, C., Mao, J., Ouyang, H., Sun, J., 2013. The genetic relationship between hydrocarbon systems and Mississippi Valley-type Zn-Pb deposits along the SW margin of Sichuan Basin, China. Int. Geol. Rev. 55, 941–957. https://doi.org/10.1080/00206814.2012.753177.

Xiong, S.F., Jiang, S.Y., Ma, Y., Liu, T., Zhao, K.D., Jiang, M.R., Zhao, H.D., 2019. Ore genesis of Kongxigou and Nanmushu Zn-Pb deposits hosted in Neoproterozoic carbonates, Yangtze Block, SW China: constraints from sulfide chemistry, fluid inclusions, and in situ S-Pb isotope analyses. Precambrian Res. 333, 105405. https://doi.org/10.1016/j.precamres.2019.105405.

Yang, C., Ni, Z., Li, M., Wang, T., Chen, Z., Hong, H., Tian, X., 2018. Pyrobitumen in South China: Organic petrology, chemical composition and geological significance. Int. J. Coal Geol. 188, 51–63. https://doi.org/10.1016/j.coal.2018.01.014.

Yao, L., Zhong, N., Khan, I., Chen, J., Luo, Q., Zhang, Y., Ai, J., Sun, W., 2021. Comparison of in-source solid bitumen with migrated solid bitumen from Ediacaran-Cambrian rocks in the Upper Yangtze region, China. Int. J. Coal Geol. 240, 103748. https://doi.org/10.1016/j.coal.2021.103748.

Ye, L., Pan, Z.P., Li, Z.Y., Liu, T.G., Sha, B., 2005. Isotopic geochemical characters in niujiaotang Cd rick znic deposit,Duyun,Guizhou. J. Mineral. Petrol. 25, 70–74. https://doi.org/10.19719/j.cnki.1001-6872.2005.02.012.

Yu, Y.S., Liu, A.S., Dai, P.Y., Zhao, W.Q., Tao, M., Liu, Z.P., 2017. The metallogenic epoch and ore-forming material source of the Tang‑ bian Pb-Zn deposit in Tongren, Guizhou Province: evidence from Rb-Sr dating of sphalerites and S-Pb isotope. Geol. Bull. China 36, 885–892.

Yuan, W.C., Li, Y.S., Zhang, G.P., Long, H.B., 1997. C, H, O and S isotope geochemistry of low-temperture Hg, Sb, au and as deposits in the Yunnan-Guizhou-Guangxi area. Acta Mineral. Sin. 4, 422–426. https://doi.org/10.16461/j.cnki.1000-4734.1997.04.008.

Zhang, T.G., Chu, X.L., Zhang, Q.R., Feng, L.J., Huo, W.G., 2004. The sulfur and carbon isotopic records in carbonates of the Dengying Formation in the Yangtze Platform, China. Acta Petrol. Sin. 20, 717–724. https://doi.org/10.3969/j.issn.1000-0569.2004.03.036.

Zhang, C.Q., Mao, J.W., Wu, S.P., Li, H.M., Liu, F., Guo, B.J., Gao, D.R., 2005. Distribution, characteristics and genesis of Mississippi Valley-Type lead_zinc deposits in Sichuan-Yunnan-Guizhou area. Mineral Deposits 24, 336–348. https://doi.org/10.3969/j.issn.0258-7106.2005.03.013.

Zhang, Q.X., Li, Z.Q., Ran, Y.L., 2007. Tectonic interpretation of the seismic profiles in the Lianhuashan area in the southern part of western Sichuan foreland basin. Sediment. Geol. Tethyan Geol. 27, 72–75. https://doi.org/10.3969/j.issn.1009-3850.2007.01.013.

Zhang, Y.X., Wu, Y., Tian, G., Shen, L., Zhou, Y.M., Dong, W.W., Zeng, R., Yang, X.C., Zhang, C.Q., 2014. Mineralization age and the source of ore-forming material at Lehong Pb-Zn Deposit, Yunnan Province: Constraints from Rb-Sr and S isotopes system. Acta Mineral. Sin. 34, 305–311. https://doi.org/10.16461/j.cnki.1000-4734.2014.03.002.

Zhao, X.Y., 1989. Stable isotope geochemistry of the Jinding lead–zinc ore deposit, Yunnan. Earth Sci. 14, 495–502.

Zhou, J.X., Huang, Z.L., Gao, J.G., Wang, T., 2012. Sources of ore-forming metals and fluid, and mechanism of mineralization, Maozu large carbonate–hosted lead–zinc deposit Northeast Yunnan Province. J. Mineral. Petrol. 32, 62–69. https://doi.org/10.19719/j.cnki.1001-6872.2012.03.009.

Zhou, Y., Duan, Q.F., Tang, J.X., Cao, L., Li, F., Huang, H.L., Gan, J.M., 2014. The Large-Scale Low-Temperature Mineralization of Lead-Zinc Deposits in Western Hunan-evidence from Fluid Inclusions. Geol. Explor. 50, 515–532. https://doi.org/10.13712/j.cnki.dzykt.2014.03.012.